Acoustic Metamaterial

Jun Xu, Navid Nemati, Nicolas Viard, Nicholas Fang, Denis Lafarge

Acoustic Metamaterial

Chapter · January 2018

DOI: 10.1142/9789813228702_0002

5 authors, including:

Jun Xu
Massachusetts Institute of Technology
34 PUBLICATIONS **1,950** CITATIONS
SEE PROFILE

Navid Nemati
Massachusetts Institute of Technology
17 PUBLICATIONS **97** CITATIONS
SEE PROFILE

Nicholas Fang
Massachusetts Institute of Technology
368 PUBLICATIONS **29,171** CITATIONS
SEE PROFILE

Denis Lafarge
Université du Maine
67 PUBLICATIONS **1,871** CITATIONS
SEE PROFILE

CHAPTER 2

Acoustic Metamaterial

JUN XU, NAVID NEMATI, NICOLAS VIARD and NICHOLAS FANG*

Massachussetts Institute of Technology, USA

DENIS LAFARGE

Laboratoire d'Acoustique de l'Université du Maine, France

2.1. Introduction

Over the past decade, electromagnetic metamaterials have shown tremendous potential in many disciplines of science and technology, and have led to a broad interest in devising techniques for manipulating different classes of waves with unconventional materials. Among them, acoustic metamaterials show the greatest promise for manipulating acoustic waves in a novel fashion for imaging, communication, detection and sound protection applications. Because of similar governing equations of electromagnetic waves and acoustic waves, which are the Maxwell equations and Helmholtz equations, respectively, the successes of metamaterials study in electromagnetic wave can be extended to the acoustic community. Permittivity and permeability of materials are used to describe electromagnetic wave properties, while acoustic wave properties are determined by

*Corresponding author: nicfang@mit.edu

Table 2.1. Analogy between electromagnetic and acoustic variables and material characteristics.

Electromagnetism (TMz)	Acoustics	Analogy
$\frac{\partial E_z}{\partial x} = -i\omega\mu_y H_y$	$\frac{\partial P}{\partial x} = -i\omega\rho_x v_x$	
$\frac{\partial E_z}{\partial y} = i\omega\mu_x H_x$	$\frac{\partial P}{\partial y} = -i\omega\rho_y v_y$	
$\frac{\partial H_y}{\partial x} - \frac{\partial H_x}{\partial y} = -i\omega\epsilon_z E_z$	$\frac{\partial v_x}{\partial x} + \frac{\partial v_y}{\partial y} = -i\omega\chi P$	
Electric field E_z	Acoustic pressure P	$P \leftrightarrow -E_z$
Magnetic field $H_x,\ H_y$	Particle velocity $v_x,\ v_y$	$v_x \leftrightarrow -H_y,\ v_y \leftrightarrow H_x$
Permittivity ϵ_z	Dynamic compressibility χ	$\chi \leftrightarrow \epsilon_z$
Permeability $\mu_x,\ \mu_y$	Dynamic density $\rho_x,\ \rho_y$	$\rho_x \leftrightarrow \mu_y,\ \rho_y \leftrightarrow \mu_x$

the mass density and compressibility of materials. Moreover, in a two-dimensional (2D) case, when there is only one polarization mode, the electromagnetic wave has scalar wave formulation. The two sets of equations for the electromagnetic and the acoustic waves in isotropic media are dual of each other by the replacement as shown in Table 2.1 and this isomorphism holds for anisotropic medium as well. Table 2.1 presents the analogy between acoustic and transverse magnetic fields in 2D under harmonic excitation. It is noted that this analogy between the electromagnetic and acoustic waves is not unique. We can also have the one-to-one mapping between the acoustic and transverse electric field. The latter analogy, which is presented in Table 2.2 for 1D propagation case (here, according to x-axis), is used, in particular, within the nonlocal description of acoustic wave propagation (see Section 2.2). From the equivalence shown in Tables 2.1 and 2.2, the desirable effective density and compressibility need to be established by structured material to realize unusual sound wave properties. Therefore, the basic question in acoustic metamaterials is to build "acoustic artificial" atoms, on a scale much smaller than

Table 2.2. Analogy between macroscopic electromagnetics and macroscopic acoustics in 1D, including temporal and spatial dispersion. Macroscopic acoustic variables are described in page 75.

Electromagnetism	Acoustics	Analogy
$\frac{\partial B_z}{\partial t} = -\frac{\partial E_y}{\partial x}$	$\frac{\partial B}{\partial t} = -\frac{\partial V_x}{\partial x}$	
$\frac{\partial D_y}{\partial t} = -\frac{\partial H_z}{\partial x}$	$\frac{\partial D_x}{\partial t} = -\frac{\partial H}{\partial x}$	
$D_y(\omega, k) = \epsilon(\omega, k)\ E_y(\omega, k)$	$D_x(\omega, k) = \rho(\omega, k)\ V_x(\omega, k)$	
$H_z(\omega, k) = \mu^{-1}(\omega, k)\ B_z(\omega, k)$	$H(\omega, k) = \chi^{-1}(\omega, k)\ B(\omega, k)$	
$S_x = E_y\ H_z$	$S_x = H\ V_x$	
Electric field E_y	Velocity field V_x	$V_x \leftrightarrow E_y$
Electric displacement field D_y	Acoustic D_x field (momentum density)	$D_x \leftrightarrow D_y$
Magnetic B_z field	Acoustic B field (condensation)	$B \leftrightarrow B_z$
Magnetic H_z field	Acoustic H field (pressure)	$H \leftrightarrow H_z$
Pointing vector (x-component) S_x	Acoustic part of energy current density S_x	$S_x \leftrightarrow S_x$
Effective permittivity $\epsilon(\omega, k)$	Effective density $\rho(\omega, k)$	$\rho \leftrightarrow \epsilon$
Effective permeability $\mu(\omega, k)$	Effective compressibility $\chi(\omega, k)$	$\chi \leftrightarrow \mu$

the relevant wavelength, to achieve effective parameters beyond the properties existing in nature.

There are several ways to design acoustic "atoms" in acoustic metamaterials. One option is to use mechanical oscillation to build deep subwavelength local resonators. Due to the resonant properties of the artificial structures, they can exhibit novel effective parameters for acoustic waves (i.e. singly or simultaneously negative mass

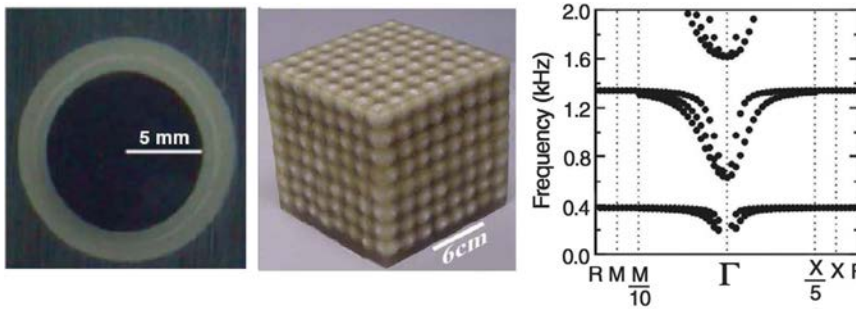

Fig. 2.1. (a) Cross section of a coated lead sphere that forms the basic man-made "atom" with local resonance; (b) Unit cells arranged in an $8 \times 8 \times 8$ sonic crystal, which is the block of acoustic metamaterial that was experimentally tested; (c) A simple cubic structure of coated spheres from 200 to 2000 Hz. Three modes (two transverse and one longitudinal) are distinguishable in the [110] direction, to the left of the Γ point. The two transverse modes are degenerate along the [100] direction, to the right of the Γ point. Note the expanded scale near the Γ point.[1]

density and compressibility) in a certain frequency range.[1–7] The effective parameters of the acoustic metamaterials can be retrieved by analyzing the acoustic wave scattering coefficients. Further studying the oscillation modes of the resonators, we can find either monopolar or dipolar resonances, which lead to negative compressibility or mass density. Some analytical analysis have been applied on simple geometries, e.g. cylindrical or spherical resonators.[8,9] Experimentally, the negative mass density has been demonstrated by immersing core-shell structures (lead core in rubber shell) in epoxy matrix,[1] as shown in Fig. 2.1. In addition, the structure of air bubble in liquid has also been explored because of the different orders of Mie scattering, which lead to monopolar or dipolar resonance at different frequencies to achieve negative compressibility or negative mass density.[4] Recently, another type of resonators — Helmholtz resonators — has been studied to demonstrate negative compressibility.[3,4,7,10,11] A typical Helmholtz resonator (as shown in Section 2.2.2, Fig. 2.3(a)) can be presented as a series of inductance and capacitance. The fluid inside the cavity is much easier to be compressed compared with that in the neck part.

Moreover, the pressure gradient along the open neck is much greater than that inside the large cavity. Therefore the cavity displays capacitive property and leaves the smaller neck as an acoustic inductor. According to the transmission line method[12] (see Section 2.2.1), the negative properties of the acoustic metamaterials can be designed by an array of subwavelength Helmholtz resonators. Experimentally, the negative compressibility was achieved in 1D Helmholtz resonator array,[3] and focusing effect by negative index acoustic metamaterial (mass density and compressibility are negative simultaneously) was demonstrated in 2D Helmholtz resonator array.[13] In addition, using the long-wavelength approximation, the effective mass density and compressibility can also be retrieved from reflection and transmission coefficients.[14,15]

Recently, a new design paradigm called conformal mapping and coordinate transformation has inspired a series of key explorations to manipulate, store and control the flow of energy, in the form of either sound, elastic waves or light radiation. In electromagnetism, because of the coordinate invariance of Maxwell's equations, the space for light can be bent in almost any arbitrary ways by providing a desired spatial distribution of electric permittivity ϵ and magnetic permeability μ.[16,17] A set of novel optical devices were proposed based on transformation optics;[18–21] they usually call for complicated medium with anisotropic and spatially varying permittivity and permeability tensors to accomplish the desired functionality. Recent advances in synthetic structured metamaterials[22,23] whose properties are determined by subwavelength structures, offer the potential to physically implement these complicated media. By modifying the shape and arrangement of these subwavelength constituent elements, anisotropy and spatial variation can be achieved in the artificial metamaterials. Due to the coordinate invariance of Helmholtz equations, the concept can be extended to the acoustic waves as well, which is called transformation acoustics. Similar to the optical metamaterials, generally, we need spatially varying mass density and compressibility tensors to manipulate the acoustic wave in the desired fashion.

The central theme of this chapter is to introduce the design and realization of acoustic metamaterials aimed at controlling and guiding acoustic waves in applications such as acoustic imaging or communication. We will first describe the approach to build an acoustic metamaterial unit cell — Helmholtz resonator — based on the transmission line model. The basic concept and derivation of lumped acoustic circuit will be introduced (Section 2.2.1). The realization of negative dynamic compressibility for the acoustic wave using Helmholtz resonator array will be demonstrated (Section 2.2.2). Newly developed nonlocal theory of the acoustic wave propagation in Helmholtz resonator array will be discussed (Section 2.2.3). By this theory, the effective medium parameters are calculated, and the behavior of the effective modulus which appears negative near the resonance will be shown to be a consequence of the nonlocal effects in this material exhibiting local resonance phenomenon. As a promising application in acoustic imaging, the lens with negative index by acoustic metamaterials will be presented (Section 2.2.4). Both the theoretical and experimental studies demonstrate the focusing of ultrasound waves through the negative index lens, which is implemented by a two-dimensional array of subwavelength Helmholtz resonators. We will also introduce a subwavelength focusing using two-dimensional Helmholtz resonator array based on strong local resonance mode (Section 2.2.5). In the next section (Section 2.3), we will focus on the realization of acoustic cloak in various ways. The design of acoustic cloak is based on transformation acoustics. The mathematical background, numerical simulation results, and experimental characterization results will be given then.

2.2. Acoustic Metamaterials Made of Helmholtz Resonators

In this section, we first review the simple principles of the acoustic transmission line method, followed by the application of the method to design metamaterials with Helmholtz resonator as the material building block. In Section 2.2.2, we describe the first application related to the one-dimensional subwavelength metamaterial, whose elastic modulus is found to be negative experimentally near

resonance frequency.[3] This metamaterial, consisting of an array of Helmhotz resonators, exhibits local resonance phenomena in the long-wavelength limit where the wavelength is much larger than the unit cell composed of one resonator. This medium property which leads to negative modulus is described precisely in Section 2.2.3, by a nonlocal theory of sound propagation taking into account the effects due to spatial dispersion and also viscothermal dissipation.[24] In Section 2.2.4, we present the focusing of a point source from a designed ultrasonic metamaterial consisting of a planar network of subwavelength Helmholtz resonators which has been experimentally investigated in Ref. 13. Transmission line method has been employed to guide us for designing this material and analysing the experimental results. In Section 2.2.5, we demonstrate the extraordinary focusing in an array of Helmholtz resonator.[25] We explain the experimental observations based on an analytical effective-medium model as well as finite-element calculations.

2.2.1. *Transmission line method*

We will review in the following an analogy which can be established between acoustic systems and electrical circuits. This analogy is based on the equivalence of the fluid motion in the acoustic system and the current in the electrical circuit. In the acoustic counterpart of the electrical circuit, acoustic capacitance and inductance can be defined in the framework of a parameter model. This model is valid when the length of the acoustic medium is much smaller than the wavelength. The effective density and compressibility of the network structure are found to be related to the capacitance and inductance in this lumped circuit.

Acoustic impedance of a tube

We consider a hollow cylindrical tube of length l and cross section area S, open at one end and closed at the other end with impedance Z. The origin of coordinates is chosen to be coinciding with the position of the open end of the tube. We assume that the diameter of the tube is sufficiently small so that the waves travel down the tube

with plane wave fronts. For an initial pressure wave traveling in the positive x direction, $p^+ = \tilde{p}^+ \exp(ikx - i\omega t)$, the reflected wave at, traveling in the negative x direction writes as $p^- = \tilde{p}^- \exp(-ikx - i\omega t)$. The corresponding particle velocity can be written as $v^+ = (\tilde{p}^+/Z_c)\exp(ikx - i\omega t)$, and $v^- = -(\tilde{p}^-/Z_c)\exp(-ikx - i\omega t)$, where $Z_c = \rho_0 c_0$ is the characteristic impedance of the fluid in the tube, and ρ_0, and c_0 are the density and sound velocity in the fluid, respectively. The total pressure and total velocity at a given position and time are $p(x,t) = p^+(x,t) + p^-(x,t)$, and $v(x,t) = v^+(x,t) + v^-(x,t)$, respectively. This yields the impedance at x

$$Z_x = \frac{p}{Sv} = \frac{Z_c}{S}\frac{\tilde{p}^+ e^{ikx} + \tilde{p}^- e^{-ikx}}{\tilde{p}^+ e^{ikx} - \tilde{p}^- e^{-ikx}} \tag{2.1}$$

We can immediately obtain the impedances Z_0 at the open end $x = 0$, and Z_l at $x = l$. This gives Z_0 as a function of Z_l

$$Z_0 = \frac{Z_c}{S}\frac{Z_l - i\frac{Z_c}{S}\tan kl}{\frac{Z_c}{S} - iZ_l \tan kl} \tag{2.2}$$

Acoustic inductance

We consider that the tube is acoustically rigid and open on both ends [Fig. 2.2(a)]. Since all quantities are in phase when the dimension of the tube is much smaller than the corresponding wavelength, the fluid moves as a whole under the action of an unbalanced force. The

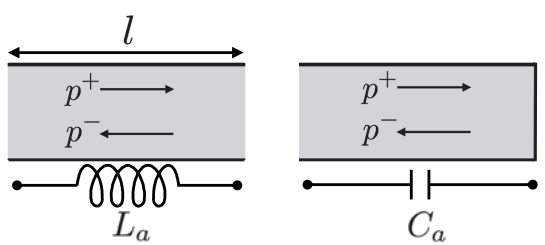

Fig. 2.2. A pipe with (a) open and (b) rigid ends is analogous to an acoustic inductor and an acoustic capacitor, respectively.

whole fluid moves without appreciable compression because of the open ends. We substitute $Z_l = 0$ in (2.2)

$$Z_0 = -i\frac{Z_c}{S}\tan kl \tag{2.3}$$

Since l is much smaller than the wavelength, kl is a small value. Therefore we can use the Taylor series to write $\tan kl = kl + \frac{(kl)^3}{3} + 2\frac{(kl)^5}{15} + \cdots$. Then (2.3) becomes $Z_0 = -i\omega\frac{\rho_0 l}{S} - i\omega^3\frac{\rho_0 l^3}{3Sc_0^2} + \cdots$. When $l < \lambda/16$, we can keep only the first term and neglect the higher order terms within about 5% error. Thus, the acoustic inductance for an open end tube can be written as

$$L_A \simeq \frac{\rho_0 l}{S} \tag{2.4}$$

Taking into account the radiation impedance, l should be replaced by an effective length of the tube l', and augmented with a correction factor: $l' = l + 8r/3\pi = l + 0.85r$, where r is the radius of the tube.

Acoustic capacitance

If the tube is rigidely closed at one end [Fig. 2.2(b)], we substitute $Z_l = \infty$ in (2.2)

$$Z_0 = i\frac{Z_c}{S}\cot kl \tag{2.5}$$

For a small value of kl, $\cot kl = \frac{1}{kl} - \frac{kl}{3} - \frac{(kl)^3}{45}$, and consequently (2.5) becomes $Z_0 = \frac{i}{\omega}\frac{1}{(V/\rho_0 c_0^2)} - i\omega\frac{l\rho_0}{3S} + \cdots$. This impedance is valid within 5% for l up to $\lambda/8$ as a combination of acoustic inductance and capacitance in series. Furthermore and as before, when $l < \lambda/16$, we can keep only the first term and neglect the higher order inductance term within about 5% error, such that the impedance

$$C_A \simeq \frac{V}{\rho_0 c_0^2} \tag{2.6}$$

where V is the volume of the tube.

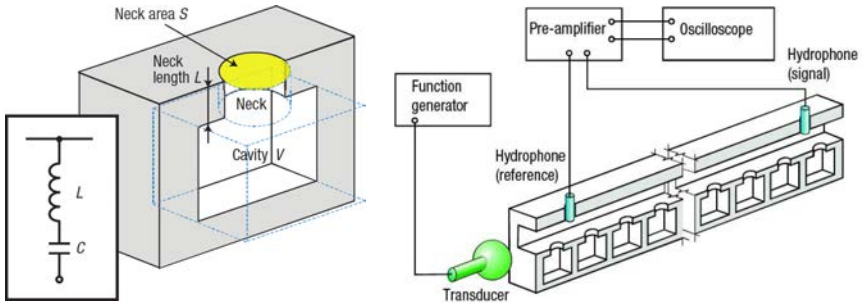

(a) (b)

Fig. 2.3. (a) Schematic cross-sectional view of a Helmholtz resonator. The sample is made of aluminum, consisting of a rectangular cavity of $3.14 \times 4 \times 5$ mm^3, and a cylindrical neck 1-mm long and 1-mm in diameter. The cavity and neck are filled with water, and are connected at the same side to a square water duct with a 4×4 mm^2 opening. The resonators are placed in a periodicity of 9.2 mm. The inset illustrates the analogy between a Helmholtz resonator and an inductor-capacitor circuit, showing the fluidic inductance due to the neck, and the acoustic capacitance due to the cavity. (b) Illustration of the setup of the ultrasonic transmission experiment.[3]

Helmholtz resonator

A typical Helmholtz resonator as in Fig. 2.3(a) can be presented as a combination of inductance and capacitance. The fluid inside the cavity is much easier to compress compared with that in the neck part. Moreover, the pressure gradient along the open neck is much greater than that inside the large cavity. Therefore, the cavity displays capacitive property and leaves the smaller neck as an acoustic inductor.

2.2.2. *Negative bulk modulus*

A new class of ultrasonic metamaterials is presented in Ref. 3 with subwavelength resonant structural units, which leads to the negative bulk modulus near the resonance. The building block of this ultrasonic metamaterial, the Helmholtz resonator, consists of a cavity of known volume with rigid walls and a small hole in one side [Fig. 2.3(a)]. The material is embedded in water, and the periodicity

is considerably smaller than the corresponding longitudinal wavelength in water ($d \simeq \lambda/5$). A pressure variation in the channel causes the plug of fluid in the hole to oscillate in and out, producing adiabatic compression and rarefaction of the liquid enclosed in the cavity. Such a resonator, as it has been mentioned above, is analogous to an inductor-capacitor circuit [Fig. 2.3(a)], with the enclosed cavity acting as the capacitor with capacitance $C \simeq V/\rho_0 c_0^2$, and the neck acting as the inductor ($L \simeq \rho_0(L'/S)$), where V is the volume of the cavity, ρ_0 is the density of water, c_0 is the sound speed in the water, L' is the effective length of the neck, and S is the cross-sectional area of the neck. Because the Helmholtz resonator does not use typical standing waves to create a resonance, the dimension of each element can be made much smaller than the acoustic wavelength (at 33 kHz, $\lambda = 4.4$ cm in water).

Following the formalism of electromagnetic response in metamaterials,[26,27] the combination of many Helmholtz resonators into a periodic array allows the material to behave as a medium with an effective modulus $\chi^{-1}(\omega)$ that can be expressed in the form

$$\chi^{-1}(\omega) = \chi_0^{-1}\left[1 - \frac{F\omega_H^2}{\omega^2 - \omega_H^2 + i\Gamma\omega}\right] \tag{2.7}$$

where $F = V/S_c d$ is a geometrical factor, S_c the cross-sectional area of the main conduit, $\omega_H = c_0\sqrt{S/L'V}$ is the resonant angular frequency, and Γ is the dissipation loss in the resonating Helmholtz elements due to viscous effects. In Fig. 2.4(a), the imaginary part of the modulus has a negative sign because the acoustic analogue of permeability corresponds to χ. This frequency dependent response is essential to the negative modulus over a range of frequencies. At frequencies near resonance, the induced displacement in the neck becomes very large, as is typical in resonance phenomena. The large response represents accumulation of energy over many cycles, such that a considerable amount of energy is stored in the resonator relative to the driving field. This stored energy is significant to maintain the sequence of displacement near resonance even when the excitation field changes the sign. That is, as the frequency of the driving

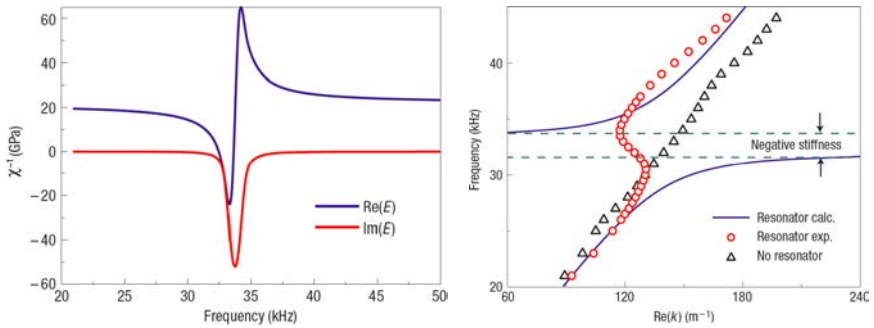

Fig. 2.4. (a) The calculated effective bulk modulus in the one-dimensional subwavelength Helmholtz resonators. (b) Measured and calculated dispersion of ultrasonic metamaterial. The red circles represent data measured from the periodical array of Helmholtz resonators in the duct, the black triangles represent the data in the duct without Helmholtz resonators, and the blue solid line is calculated using a sum of lossless Bloch waves.[3]

pressure field is swept through the resonance, the instantaneous velocity of the mass centre in the unit cell flips from in-phase to out-of-phase with the driving field, and the material shows a negative response. Similarly, a polariton effect is also observed in the electromagnetic response of metamaterials, where a negative permittivity or permeability (generally on the higher frequency side of the resonance) implies a purely imaginary wavevector in the bulk medium. Here, this idea has been implemented in the context of elastic composites at ultrasonic frequencies. By varying the size and geometry of the structural unit, we can tune the effective elastic moduli to negative values at desired frequency ranges.

Theory on the lossless resonators predicts that a full bandgap opens up between 32 and 34 kHz, whereas away from this dip the dispersion behaves linearly. However, experimental data show that possible propagation modes can exist in the bandgap with a backbending of the dispersion curve, which suggests an antiparallel relation between group and phase velocities. This is a direct result of the loss in the system. When ultrasonic metamaterials approach resonance, the complex modulus $\chi^{-1} = -|\Re(\chi^{-1})| + i\Im(\chi^{-1}) =$

$-\alpha - i\beta$ is expected in the spectral dip as a result of friction dissipation ($\alpha, \beta > 0$ as shown in Fig. 2.4(b)), where $\Im(\chi^{-1})$ indicates the imaginary part, and α, β are parameters corresponding to the real and imaginary parts of the complex modulus. It is straightforward to write the propagation constant in the system as $k = (-\alpha + i\beta)^{1/2}\omega\sqrt{\rho_0/(\alpha^2+\beta^2)}$, with a small real component

$$\Re(k) = -\frac{\omega}{2}\sqrt{\frac{\rho_0}{\alpha^2+\beta^2}}\left\{\sqrt{\alpha^2+\beta^2}-\alpha\right\}^{1/2} \tag{2.8}$$

characterizing a propagating mode in the bandgap, whereas the imaginary part

$$\Im(k) = +\frac{\omega}{2}\sqrt{\frac{\rho_0}{\alpha^2+\beta^2}}\left\{\sqrt{\alpha^2+\beta^2}+\alpha\right\}^{1/2} \tag{2.9}$$

describes the decaying length of the pulse. The dispersion of these complex wavevectors can be well captured in our experiment by sweeping in real frequencies. Taking into account a small propagating component as an effect of resonant re-emission in parallel to the dominant tunnelling process in the transmission dip, the dispersion relationship can be characterized in the experimental results [Fig. 2.4(b)]. In addition, as frequency increases above the band edge, the attenuation (β) increases leading to the reduction of the real wavevector $\Re(k)$, resulting in the back-bending of the dispersion curve observed in Fig. 2.4(b). The loss term ($\Gamma = 2\pi \times 400$ Hz) is determined empirically by fitting the calculated transmission data along the edges of the experimental expectral dip.[3]

2.2.3. *Nonlocal description of sound propagation*

We employ here a generalized macroscopic nonlocal theory of sound propagation in rigid-framed porous media saturated with a viscothermal fluid[28] to describe the behavior of an acoustic metamaterial made of an array of Helmholtz resonators filled with air [see Fig. 2.5(a)].[24] Inspired by the electromagnetic theory and a thermodynamic consideration relating to the concept of acoustic part of energy current density, this macroscopic theory allows us to go beyond the limits of

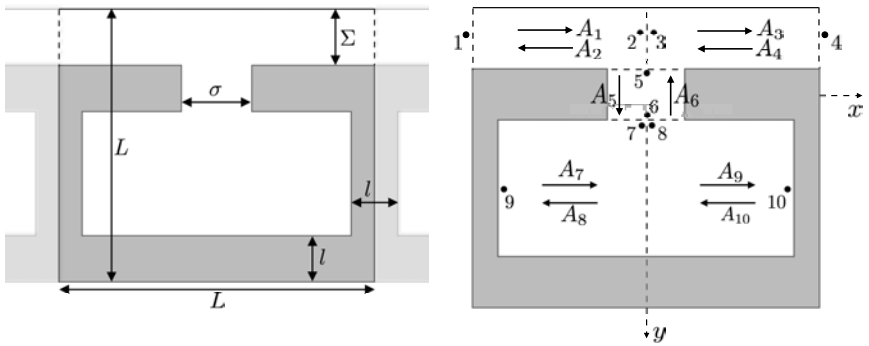

Fig. 2.5. (a): A unit cell in a 2D array of Helmholtz resonators. The dimensions are $L = 1\ cm$, $\Sigma = 0.2\ L$, $\sigma = 0.015\ L$, and $l = 0.15\ L$. (b): Illustration of slit portions and plane waves propagating in different parts of the resonator. Different positions are indicated by m, and different amplitudes by A_m, $m = 1, \ldots, 10$.

the classical local theory and within the limits of linear theory, to take into account temporal and spatial dispersion. By *macroscopic theory* we mean that the theory is concerned with averaged fields only. Assuming that there is a suitable ensemble of realizations of the medium, the macroscopic theory then is developed to describe the dynamics of the ensemble-averaged fields. A special case will be that of a periodic medium. The ensemble will be the collection of configurations generated by random translations of a single sample, and the ensemble average will be related to cell average of one sample. In the framework of the new approach, a homogenization procedure is proposed, through solving two independent microscopic action-response problems each of which related to the effective density and effective bulk modulus of the material. Contrary to the classical (two-scale asymptotic) method of homogenization, no asymptotic approach has been employed and there is no length-constraint to be considered within the development of the new method. Thus, there would be no frequency limit for the medium effective properties to be valid; in addition, materials with different length scales can be treated. The homogenization procedure offers a systematic way of obtaining the effective properties of the materials, regardless of their geometries.

These characteristics of the nonlocal approach permits the description of the porous media with specific geometries causing metamaterial behavior. A metamaterial with periodic structure will be studied: two-dimensional array of Helmholtz resonators connected in series.

By local theory, we refer to space locality. Nonlocality in time, or temporal dispersion, has been already taken into account through models for wave propagation in porous media.[29–32] That is, in Fourier space the effective density and bulk modulus depend on the frequency ω. In other words, the field dynamics at one location retains a memory of the field values at this location but is not affected by the neighboring values. The local description is usually based on retaining only the leading order terms in the two-scale homogenization method.[32–38] An asymptotic two-scale approach is applied in terms of a characteristic length of the medium, the period L in periodic media, which is assumed to be much smaller than the wavelength λ.[39,40] Efforts have been performed to extend the asymptotic method of homogenization to higher frequencies for the periodic composite materials[41,42] and rigid porous media[43] by introducing another type of scale separation to which the asymptotic multi-scale procedure applies. An enhanced asymptotic method has been adapted to describe sound propagation in rigid porous media with embedded damped Helmholtz resonators[44] exhibiting scattering different from Bragg scattering at high frequency in periodic media.

An effective medium approach has been proposed for periodic elastic composites based on surface responses of a structural unit of the material,[45] which can describe the macroscopic parameters beyond the frequencies within the long wavelength limit. Unlike the classical methods, based on the introduction of two-scale asymptotic expansions, or coherent potential approximation[46] based on the effective-medium parameters minimizing scatterings in the long-wavelength limit, the homogenization scheme presented in Ref. 45 uses matching the lowest-order scattering amplitudes arising from a periodic unit cell of the metamaterial with that of a homogenized material. As such, local resonant scattering can be captured as well

by the latter method in the elastic metamaterials. The asymptotic method of homogenization has been enhanced to provide the weak nonlocal effects as a small correction to the local behavior.[47] An approach has been presented[48] for random elastic composites based on ensemble averaging of the material responses to a body force, giving rise to effective parameters of the medium depending on frequency and wavenumber. By this method, the case of periodic media can be treated as well.

The nonlocal theory we use here takes fully the temporal dispersion and spatial dispersion into account. The medium is assumed unbounded and homogeneous in the stationary random statistical sense; therefore, the spatial dispersion refers only to the dependence of the permittivities, i.e. effective density and bulk modulus, on the Fourier wavenumbers $\boldsymbol{k}$ present in the macroscopic fields.[49] As mentioned above, the theory can be applied with certain considerations to a periodic medium; in particular it gives the Bloch wavenumbers and defines Bloch impedances. The materials susceptible to showing the nonlocal behavior may be classified into two main groups regarding their microgeometry. The first comprises the materials which exhibit this behavior in sufficiently high frequency regime. The second one concerns materials with microgeometry constituting the resonators, which exhibit spatial dispersion phenomena even at not very high frequencies; the resonance phenomena act as a source generating nonlocal behavior. In this article, we investigate the second type of these geometries in the form of daisy-chained Helmholtz resonators. A material made of an array of Helmholtz resonators filled by water has been studied experimentally, and has been found to show negative bulk modulus in the resonance frequency range[3] (see Section 2.2.2). Later, Helmhotz resonators as structural units were used to design novel metamaterials for focusing ultrasound waves[13] (see Section 2.2.4 and broadband acoustic cloaking[50]).

Here, we apply the nonlocal theory to quantatively describe the macroscopic dynamics of such a metamaterial filled with air as a viscothermal fluid, in 2D. Using a simplified analytical solution of the complete equations, we present the method of obtaining the

nonlocal efffective density and effective bulk modulus. When these effective parameters satisfy the dispersion equation based on the nonlocal theory, we can compute the wavenumber of the least attenuated mode, among other modes. We can then check that the wavenumber resulting from the macroscopic nonlocal theory coincides with the wavenumber associated with the Bloch wave propagating and attenuating in the medium. The Bloch solution is determined using the same simplifying way of solving as in the nonlocal modeling. Thus the results based on the two calculations should be comparable. Finally, as a check of the validity of the simplifying assumptions introduced in our modeling calculations, we have performed direct Finite Element Method (FEM) computations based on the exact equations in the framework of nonlocal homogenization.

First, we review briefly the general framework of the nonlocal theory which is used in this section. The microscopic equations governing sound propagation in a rigid porous medium are summarized, before mentioning the macroscopic Maxwellian equations describing the macroscopic nonlocal dynamics of the homogenized equivalent fluid. Then, we will see the nonlocal modeling allowing the calculation of the effective parameters and the wavenumber of the least attenuated wave in the medium. The direct calculation of the Bloch wavenumber, using similar simplifications, is presented next, followed by the results and analysis of the three different calculations.

General Framework of the Nonlocal Theory

In the following, we state the microscopic equations applied at the pore level, and the nonlocal Maxwellian macroscopic equations that describe the dynamics of the material as a homogeneous equivalent fluid medium. Then, we recall briefly the upscaling procedures allowing to obtain the frequency and wavenumber dependent effective parameters of the macroscopic equivalent fluid medium, i.e. effective density and effective bulk modulus. This section is a summary of the results which have been discussed in detail in Ref. 28. Hence, we will frequently refer to Ref. 28, for the in-depth explanations.

Microscopic Equations

The dynamics of a small amplitude perturbation in a rigid-framed porous material filled with a viscothermal fluid is governed by the linearized equations of the mass, momentum, and energy balance, and a general fluid state equation as follows: in the fluid region $\mathcal{V}^f$

$$\rho_0 \frac{\partial \boldsymbol{v}}{\partial t} = -\boldsymbol{\nabla} p + \eta \boldsymbol{\nabla}^2 \boldsymbol{v} + \left(\zeta + \frac{\eta}{3}\right) \boldsymbol{\nabla}(\boldsymbol{\nabla} \cdot \boldsymbol{v}) \tag{2.10a}$$

$$\frac{\partial b}{\partial t} + \boldsymbol{\nabla} \cdot \boldsymbol{v} = 0 \tag{2.10b}$$

$$\gamma \chi_0 p = b + \beta_0 \tau \tag{2.10c}$$

$$\rho_0 c_p \frac{\partial \tau}{\partial t} = \beta_0 T_0 \frac{\partial p}{\partial t} + \kappa \boldsymbol{\nabla}^2 \tau \tag{2.10d}$$

where $\boldsymbol{v}$, $b \equiv \rho/\rho_0$, p and τ, are the fluid velocity, excess condensation, thermodynamic excess pressure, excess temperature, respectively, and ρ is the excess density. The fluid constants ρ_0, η, ζ, γ, χ_0, β_0, c_p, T_0, κ, represent the ambient density, first viscosity, second viscosity, ratio of the heat capacity at constant pressure to heat capacity at constant volume c_p/c_v, adiabatic compressibility, coefficient of thermal expansion, specific heat capacity per unit mass at constant pressure, ambient temperature, and coefficient of thermal conduction, respectively.

In the (rigid) solid phase region $\mathcal{V}^s$, energy balance equation is reduced to $\rho^s c_p^s (\partial \tau^s/\partial t) = \kappa^s \boldsymbol{\nabla}^2 \tau^s$, where ρ^s is the constant solid density, τ^s solid excess temperature, and κ^s solid coefficient of thermal conductivity. On the fluid/solid interface $\partial\mathcal{V}$, we have the conditions of continuity of the excess temperature $\tau = \tau^s$ and the heat flux $\kappa \boldsymbol{\nabla} \tau = \kappa^s \boldsymbol{\nabla} \tau^s$. We admit that the coefficient of thermal conductivity of the solid is much larger than that of the fluid $\kappa^s \gg \kappa$, and the heat capacity at constant pressure of the solid part is much larger than that of the fluid part, i.e., $(1-\phi)\rho^s c_p^s \gg \phi \rho_0 c_p$; where ϕ is the fluid volume fraction (porosity). The latter assumptions combined with the Fourier heat diffusion in the solid, and the temperature and heat flux continuity relations, generally result in the vanishing of the

fluid excess temperature at the fluid/solid boundaries. In addition, we assume no-slip condition on the fluid/(rigid) solid interface. The boundary conditions for the velocity and excess temperature on $\partial\mathcal{V}$ are finally written as

$$\boldsymbol{v} = 0, \quad \tau = 0 \tag{2.11}$$

Macroscopic Maxwellian Acoustics

Before going through the macroscopic equations for sound propagation in rigid-framed porous media, and the homogenization procedure, we will precise the notion of field averaging in the nonlocal approach.

Averaging: The present macroscopic theory is statistical in nature and has been developed in principle for fluid-saturated rigid-framed media which are homogeneous in an ensemble-averaged sense; this is the case of stationnary random media. The macroscopic properties represented in the theory refer to the ensemble of realizations. Thus, for example, the propagation constants of the medium would refer to the propagation constant of *coherent waves* in multiple-scattering theory. Here, the material we wish to study is not defined by stationary random realizations. It belongs to the important class of periodic materials. The macroscopic theory can still be applied by considering the ensemble obtained through random translation of one sample. It turns out that the ensemble-average $\langle\ \rangle$ properties of the space are, in this case, precisely computable by spatial averaging over a periodic cell in a single realization. This, in a sense, reminds of *ergodicity* in stationary random media.

The macroscopic condensation and velocity are defined as the average of pore scale microscopic fields: $\boldsymbol{V} \equiv \langle \boldsymbol{v} \rangle$, and $B \equiv \langle b \rangle$; average over the periodic cell in the case of the periodic media. A macroscopic equation can be obtained directly by averaging Eq. (2.10b), using the commutation relation $\langle \boldsymbol{\nabla}.\boldsymbol{v} \rangle = \boldsymbol{\nabla}.\langle \boldsymbol{v} \rangle$ which is automatically satisfied owing to (2.11) (see Eq. (56) in Ref. 28). The second macroscopic field equation, as well as the macroscopic constitutive relations, are written using the electromagnetic analogy. This analogy suggests that the system of macroscopic equations can be carried

through by introducing new Maxwellian fields H and $\boldsymbol{D}$, as well as linear operators $\hat{\rho}$ and $\hat{\chi}^{-1}$. The field equations and constitutive relations are written as (see Section 3.3 in Ref. 28)

$$\textbf{Field equations:} \qquad \frac{\partial B}{\partial t} + \boldsymbol{\nabla} \cdot \boldsymbol{V} = 0, \qquad \frac{\partial \boldsymbol{D}}{\partial t} = -\boldsymbol{\nabla} H \tag{2.12}$$

$$\textbf{Constitutive relations:} \quad \boldsymbol{D} = \hat{\rho} \boldsymbol{V}, \qquad H = \hat{\chi}^{-1} B \tag{2.13}$$

where the integral operators of density $\hat{\rho}$ and bulk modulus $\hat{\chi}^{-1}$ are such that

$$\boldsymbol{D}(t, \boldsymbol{r}) = \int_{-\infty}^{t} dt' \int d\boldsymbol{r}' \rho(t - t', \boldsymbol{r} - \boldsymbol{r}') \boldsymbol{V}(t', \boldsymbol{r}') \tag{2.14a}$$

$$H(t, \boldsymbol{r}) = \int_{-\infty}^{t} dt' \int d\boldsymbol{r}' \chi^{-1}(t - t', \boldsymbol{r} - \boldsymbol{r}') B(t', \boldsymbol{r}') \tag{2.14b}$$

We notice that the kernels ρ and χ^{-1} depend on the difference $t - t'$ and $\boldsymbol{r} - \boldsymbol{r}'$, which is due to the homogeneity of the medium with respect to time and space. Therefore, we can write (2.14a) and (2.14b) in the Fourier space, respectively, as

$$\boldsymbol{D}(\omega, \boldsymbol{k}) = \rho(\omega, \boldsymbol{k}) \boldsymbol{V}(\omega, \boldsymbol{k}), \quad H(\omega, \boldsymbol{k}) = \chi^{-1}(\omega, \boldsymbol{k}) B(\omega, \boldsymbol{k}) \tag{2.15}$$

provided that

$$\rho(t - t', \boldsymbol{r} - \boldsymbol{r}') = \int \frac{d\omega}{2\pi} \frac{d\boldsymbol{k}}{(2\pi)^3} \, \rho(\omega, \boldsymbol{k}) \, e^{-i\omega(t-t') + i\boldsymbol{k}.(\boldsymbol{r}-\boldsymbol{r}')}$$

$$\chi^{-1}(t - t', \boldsymbol{r} - \boldsymbol{r}') = \int \frac{d\omega}{2\pi} \frac{d\boldsymbol{k}}{(2\pi)^3} \, \chi^{-1}(\omega, \boldsymbol{k}) \, e^{-i\omega(t-t') + i\boldsymbol{k}.(\boldsymbol{r}-\boldsymbol{r}')}$$

In other words, because of the medium homogeneity with respect to time and space, $\boldsymbol{D}(\omega, \boldsymbol{k})$ is related to $\boldsymbol{V}(\omega, \boldsymbol{k})$, and $H(\omega, \boldsymbol{k})$ is related to $B(\omega, \boldsymbol{k})$, for the same values of ω and $\boldsymbol{k}$.

In nonlocal theory, the macroscopic H field is defined through the Poynting-Schoch condition of *acoustic part of energy current density*[28,51] which is postulated as (see Section 3.4 in Ref. 28)

$$S = H\boldsymbol{V} = \langle p\boldsymbol{v} \rangle \tag{2.16}$$

As a result of this definition, the density and bulk modulus operators become susceptibility functions determinable, in principle, through independent action-response problems (see Section 2.4 in Ref. 28). Regarding Eqs. (2.14) and (2.15), it is visible that the theory allows for both temporal dispersion, shown by integration over time variable t' in physical space and frequency dependence in Fourier space, and spatial dispersion, shown by integration over space coordinates $\boldsymbol{r}'$ and wavenumber dependence in Fourier space. We will recognize the quantities in physical space $(t, \boldsymbol{r})$ and Fourier space $(\omega, \boldsymbol{k})$ by their arguments. Now, in order to clarify the relationship between constitutive operators and microgeometry, the kernel functions $\rho(\omega, \boldsymbol{k})$ and $\chi^{-1}(\omega, \boldsymbol{k})$ are needed to be determined, by introducing action-response procedures coarse-graining the dissipative fluid dynamics of the pore scale.

Procedures to Compute Effective Density and Bulk Modulus

In the 1D case of macroscopic propagation along a symmetry axis, for instance x-axis with the unit vector $\hat{\boldsymbol{x}}$, we will have $\boldsymbol{D} = D\hat{\boldsymbol{x}}$ and $\boldsymbol{V} = V\hat{\boldsymbol{x}}$, $\boldsymbol{r} = x\hat{\boldsymbol{x}}$, and $\boldsymbol{k} = k\hat{\boldsymbol{x}}$ in the above equations (2.12–2.16). To determine the Fourier functions $\rho(\omega, k)$ and $\chi^{-1}(\omega, k)$ for the 1D acoustic propagation in a medium with porosity ϕ, we solve two independent action-response problems (see Section 4 in Ref. 28). For computing the effective density we consider the macroscopic response of the fluid subject to a single-component (ω, k) Fourier bulk force. The effective bulk modulus is related to the response of the fluid subject to a single-component Fourier rate of heat supply.

Two sets of equations to be solved

The two systems of equations to be solved are written as

In the fluid region $\mathcal{V}_f$:

$$\frac{\partial b}{\partial t} + \boldsymbol{\nabla} \cdot \boldsymbol{v} = 0 \tag{2.17a}$$

$$\rho_0 \frac{\partial \boldsymbol{v}}{\partial t} = -\boldsymbol{\nabla} p + \eta \boldsymbol{\nabla}^2 \boldsymbol{v} + \left(\zeta + \frac{1}{3}\eta\right) \boldsymbol{\nabla} (\boldsymbol{\nabla} \cdot \boldsymbol{v}) + \underbrace{\boldsymbol{F} e^{-i\omega t + ikx}}_{\text{Added for determination of density}} \tag{2.17b}$$

$$\rho_0 c_p \frac{\partial \tau}{\partial t} = \beta_0 T_0 \frac{\partial p}{\partial t} + \kappa \boldsymbol{\nabla}^2 \tau + \underbrace{\dot{Q} e^{-i\omega t + ikx}}_{\text{Added for determination of bulk modulus}} \tag{2.17c}$$

$$\gamma \chi_0 p = b + \beta_0 \tau \tag{2.17d}$$

On the fluid/solid interface $\partial\mathcal{V}$:

$$\boldsymbol{v} = 0, \quad \tau = 0 \tag{2.18}$$

For convenience the excitation amplitudes are written as: $\dot{Q} e^{-i\omega t + ikx} = \beta_0 T_0 (\partial/\partial t)(\mathcal{P} e^{-i\omega t + ikx})$, and $\boldsymbol{F} e^{-i\omega t + ikx} = -\boldsymbol{\nabla}(\mathcal{P} e^{-i\omega t + ikx})$. Here, it is important to note that the excitation variables ω and k are set as independent variables. The solutions to the above systems for the fields p, b, τ, and components of $\boldsymbol{v}$ take the form $p(t, \boldsymbol{r}) = p(\omega, k, \boldsymbol{r}) e^{-i\omega t + ikx}$, and so on. Recall that the theory is formulated for a geometry that is stationary random, and the averaging operator $\langle\ \rangle$ refers to the ensemble averaging. Thus, here, the amplitude fields $\boldsymbol{v}(\omega, k, \boldsymbol{r})$, $p(\omega, k, \boldsymbol{r})$, $b(\omega, k, \boldsymbol{r})$, and $\tau(\omega, k, \boldsymbol{r})$, are stationary random functions of $\boldsymbol{r}$. Passing to the case of periodic geometry, we can limit ourselves to considering one periodic sample. The fields become periodic functions over a cell, and $\langle\ \rangle$ is interpreted as a volume average over a cell.

Frequency and Wavenumber Dependent Effective Density and Bulk Modulus

Once the two systems of equations are solved independently, using the right hand Maxwellian macroscopic equations in (2.12) and

(2.13), we arrive at the following expressions for the nonlocal effective density and bulk modulus

$$\rho(\omega,k) = \frac{k\left(\mathcal{P} + P(\omega,k)\right)}{\omega\left\langle v(\omega,k,\boldsymbol{r})\right\rangle} \tag{2.19a}$$

$$\chi^{-1}(\omega,k) = \frac{P(\omega,k) + \mathcal{P}}{\langle b(\omega,k,\boldsymbol{r})\rangle + \phi\gamma\chi_0\mathcal{P}} \tag{2.19b}$$

where $P\langle \boldsymbol{v}\rangle = \langle p\boldsymbol{v}\rangle$, which has been inspired by (2.16).

Wavenumbers, Constants of the Medium

Contrary to the case of local theory, here, since we fully take into account spatial dispersion, several normal mode solutions might exist, with fields varying as $e^{-i\omega t+ikx}$. Solutions should satisfy the following dispersion equation

$$\rho(\omega,k)\chi(\omega,k)\omega^2 = k^2 \tag{2.20}$$

which is easily derived from the Maxwellian macroscopic equations. With each frequency ω, several complex wavenumbers $k_n(\omega)$, $\Im(k_n) > 0$, $n = 1, 2, \ldots$, may be associated.

Frequency Dependent Effective Parameters

With each wavenumber k_n solution of the nonlocal dispersion equation (2.20) are associated a frequency-dependent density and bulk-modulus, such that

$$\rho_n(\omega) = \rho_n(\omega, k_n(\omega)) \tag{2.21a}$$

$$\chi_n^{-1}(\omega) = \chi_n^{-1}(\omega, k_n(\omega)) \tag{2.21b}$$

The fact that at each frequency ω, we can obtain several modes propagating and attenuating in the medium, with wavenumbers $k_n(\omega)$ constants of the medium, and effective parameters $\rho_n(\omega)$ and $\chi_n^{-1}(\omega)$, is a direct consequence of the nonlocal description. In other words, the existence of multiple wavenumbers at each frequency, associated with unique effective parameters, is a signature of the nonlocal effects or spatial dispersion in the medium. In what

follows, with the aim of obtaining the nonlocal effective density $\rho_1(\omega)$, effective bulk modulus $\chi_1^{-1}(\omega)$, and wavenumber k_1 of the least attenuated mode, we will apply this theoretical framework in analytical simplified manner, to a 2D array of Helmholtz resonators, illustrated in Fig. 2.5(a). Sound propagation through this material exhibits resonance phenomena resulting in metamaterial behavior.

Nonlocal Modelling

For 2D structures, we proceed to determine the functions $\rho(\omega, k)$ and $\chi^{-1}(\omega, k)$ sufficiently precise to give an appropriate modeling of the least attenuated mode, which results then in purely frequency dependent functions $\rho(\omega)$ and $\chi^{-1}(\omega)$. For this purpose, we do not need to consider in full detail the microscopic fields $\boldsymbol{v}$ and p. In the waveguide t and cavity c, instead of the microscopic fields, we can use the mean values $V_{t(c)} = \langle \boldsymbol{v} \rangle_S \cdot \hat{\boldsymbol{x}}$ and $P_{t(c)} = \langle p \rangle_S$, where $\langle\ \rangle_S$ denotes the average at a given x over the waveguide or the cavity width; and in the neck n, we can use the mean values $V_n = \langle \boldsymbol{v} \rangle_S \cdot \hat{\boldsymbol{y}}$ and $P_n = \langle p \rangle_S$, where $\langle\ \rangle_S$ denotes the average at a given y over the neck width, and $\hat{\boldsymbol{y}}$ is the unit vector in the y direction. At the same time, we make some simplifications consistent with describing the propagation of these averaged quantities in terms of the Zwikker and Kosten densities $\rho(\omega)$ and bulk moduli $\chi^{-1}(\omega)$, in the different slit portions. These depend only on the slit half-widths, which we shall denote by s_t, s_n, and s_c, in the tube, neck, and cavity, respectively. The different slit-like tube portions are illustrated in Fig. 2.5(b). The main tube t is divided in two Zwikker and Kosten ducts, a left duct, and a right duct, oriented in the x direction. The same separation is made for the cavity c, whereas the neck n is not divided but viewed as one Zwikker and Kosten duct oriented in y direction.

Determination of nonlocal effective density

Considering the periodic cell of Fig. 2.5(a), and the corresponding cell average operation $\langle\ \rangle$, we look for the response of the fluid when

a harmonic driving force $f(t,x) = fe^{-i\omega t+ikx}$ in the direction of $\hat{\boldsymbol{x}}$ is applied. If we can determine the microscopic response velocity and pressure fields $\boldsymbol{v}$, p, then we will have the function $\rho(\omega,k)$ through the relation (see Eq. (2.19a))

$$\rho(\omega,k) = \frac{f - ik\mathtt{P}(\omega,\mathtt{k})}{-i\omega\langle v(\omega,k,\boldsymbol{r})\rangle} \tag{2.22}$$

with $\mathtt{P}(\omega,k) = \langle pv\rangle/\langle v\rangle$, where the v is the x-component of the microscopic velocity $\boldsymbol{v}$.

In [51, Appendix], the Zwikker and Kosten local theory is expressed for tubes of circular cross-section. For 2D slits, exactly the same general principles of modeling may be used; only some details of the calculations are changed. In particular, the Bessel functions J_0 and J_1 are replaced by cosh and sinh functions. Zwikker and Kosten's effective densities $\rho_\alpha(\omega)$ and bulk modulii $\chi_\alpha^{-1}(\omega)$ in the guide, neck and cavity, will be[52]

$$\rho_\alpha(\omega) = \rho_0\left[1 - \frac{\tanh\left(\sqrt{-i\omega\rho_0 s_\alpha^2/\eta}\right)}{\sqrt{-i\omega\rho_0 s_\alpha^2/\eta}}\right]^{-1} \tag{2.23a}$$

$$\chi_\alpha^{-1}(\omega) = \gamma P_0\left[1 + (\gamma-1)\frac{\tanh\left(\sqrt{-i\omega\rho_0 c_p s_\alpha^2/\kappa}\right)}{\sqrt{-i\omega\rho_0 c_p s_\alpha^2/\kappa}}\right]^{-1} \tag{2.23b}$$

for $\alpha = t,n,c$, where the indexes t, n, and c are related to the tube, neck, and cavity, respectively; P_0 the fluid pressure at rest. The corresponding wavenumbers $k_\alpha(\omega)$ and characteristic admittances $Y_\alpha(\omega)$ are expressed as $k_\alpha = \omega/c_\alpha$, and $Y_\alpha(\omega) = 2s_\alpha/(\rho_\alpha c_\alpha)$, for $\alpha = t,n,c$, where $c_\alpha = 1/\sqrt{\rho_\alpha\chi_\alpha}$, is the corresponding Zwikker and Kosten's phase velocity. Notice that we include the slit width $2s_\alpha$ (resp. Σ,σ, and $L-\Sigma-2l$ in the resonator, see Fig. 2.5(a)) in the definition of the characteristic admittance, because it simplifies the subsequent writing of continuity conditions.

We start writing the Zwikker and Kosten's equations in the different parts of the periodic cell. For the tube and the cavity, i.e., $\alpha = t, c$, we have

$$-i\omega\frac{\rho_\alpha(\omega)}{S_\alpha}V_\alpha = -\frac{\partial P_\alpha}{\partial x} + fe^{ikx} \tag{2.24a}$$

$$i\omega S_\alpha \chi_\alpha(\omega) P_\alpha = \frac{\partial V_\alpha}{\partial x} \tag{2.24b}$$

where, $V_\alpha = V_x S_\alpha$ is the flow rate field across the cross section S_α, with V_x the x-component of the velocity in the sense of Zwikker and Kosten (averaged over the section), and P_α is the Zwikker and Kosten's pressure. In the neck, the external excitation having no y-component, we have

$$i\omega\frac{\rho_n(\omega)}{\sigma}V_n = \frac{\partial P_n}{\partial y} \tag{2.25a}$$

$$i\omega\sigma\chi_n(\omega)P_n = \frac{\partial V_n}{\partial y} \tag{2.25b}$$

where, $V_n = V_y\sigma$ is the flow rate, with V_y the y-component of the velocity, and P_n is the Zwikker and Kosten's pressure in the neck.

The general solution of the non homogeneous equations in the tube and the cavity, (P_α, V_α), $\alpha = t, c$, is written as the sum of the general solution $(P_{\alpha,h}, V_{\alpha,h})$ of the homogeneous equations and a particular solution $(P_{\alpha,p}, V_{\alpha,p})$ of the non homogeneous equations. A general solution of the homogeneous equations (2.24) is written as

$$\begin{pmatrix} P_{\alpha,h} \\ V_{\alpha,h} \end{pmatrix} = \begin{pmatrix} 1 \\ Y_\alpha \end{pmatrix} A^+ e^{ik_\alpha x} + \begin{pmatrix} 1 \\ -Y_\alpha \end{pmatrix} A^- e^{-ik_\alpha x} \tag{2.26}$$

where A^+ and A^- are the amplitudes of the plane waves in direction of the positive x-axis and negative x-axis, respectively. The following particular solution can be considered

$$\begin{pmatrix} P_{\alpha,p} \\ V_{\alpha,p} \end{pmatrix} = \begin{pmatrix} B_\alpha \\ C_\alpha \end{pmatrix} fe^{ikx} \tag{2.27}$$

where B_α and C_α represent four constants (for each ω) to be determined. Substituting (2.27) in (2.24) gives the four constants $B_t =$

$ik/(\omega^2\rho_t\chi_t - k^2)$, $C_t = i\omega\chi_t\Sigma/(\omega^2\rho_t\chi_t - k^2)$, $B_c = ik/(\omega^2\rho_c\chi_c - k^2)$, and $C_c = i\omega\chi_c(L - \Sigma - 2l)/(\omega^2\rho_c\chi_c - k^2)$. The particular solution is the same in the left and right portions of the tube and the cavity. On the contrary and because of the presence of the neck, the general solution will have different amplitude constants in the left and right portions. Thus, the general solution of Eqs. (2.24) can be written as

$$\begin{pmatrix} P_t \\ V_t \end{pmatrix} = \begin{pmatrix} 1 \\ Y_t \end{pmatrix} A_{1,3} f e^{ik_t x} + \begin{pmatrix} 1 \\ -Y_t \end{pmatrix} A_{2,4} f e^{-ik_t x} + \begin{pmatrix} B_t \\ C_t \end{pmatrix} f e^{ikx} \tag{2.28a}$$

$$\begin{pmatrix} P_c \\ V_c \end{pmatrix} = \begin{pmatrix} 1 \\ Y_c \end{pmatrix} A_{7,9} f e^{ik_c x} + \begin{pmatrix} 1 \\ -Y_c \end{pmatrix} A_{8,10} f e^{-ik_c x} + \begin{pmatrix} B_c \\ C_c \end{pmatrix} f e^{ikx} \tag{2.28b}$$

where (2.28a) with amplitudes A_1 and A_2 corresponds to the left part of the tube, and with amplitudes A_3 and A_4 to the right part [Fig. 2.5(b)]; similarly for (2.28b): A_7 and A_8 for the left part of the cavity, and A_9 and A_{10} for the right part [Fig. 2.5(b)]. These eight amplitudes are to be determined. The general solution of Eqs. (2.25), (P_n, V_n) has the form

$$\begin{pmatrix} P_n \\ V_n \end{pmatrix} = \begin{pmatrix} 1 \\ Y_n \end{pmatrix} A_5 f e^{ik_n y} + \begin{pmatrix} 1 \\ -Y_n \end{pmatrix} A_6 f e^{-ik_n y} \tag{2.29}$$

where A_5 and A_6 are the neck amplitude-relating constants to be determined (Fig. 2.5(b)).

Indeed, in the framework of our simple plane-wave modeling, there are 10 relations concerning the flow rate and pressure, which are assumed to be verified. These continuity relations involve the values of the fields at different locations indicated by numbers $m = 1, \ldots, 10$, in Fig. 2.5(b). As such, we have 10 equations for 10 unknown amplitudes $A_1, \ldots, A_{10}$.[24] Once these are determined, we will have all the Zwikker and Kosten's fields through Eqs. (2.28) and (2.29). At this point, we can easily obtain the cell averages $\langle v \rangle$ and $\langle pv \rangle$, regarding the fact that the Zwikker and Kosten's flow rate has no component along the y-axis.[24] Subsequently, we can obtain

explicitly the effective density function $\rho(\omega, k)$ through Eq. (2.22). In the next section, the effective bulk modulus is computed in a similar way but with a different excitation term, and with exactly the same conditions on the flow rate and pressure fields at different junctions.

Determination of nonlocal effective bulk modulus

Considering the periodic cell [Fig. 2.5(b)], when a harmonic heating $\dot{Q}(t,x) = \dot{Q}_0 e^{-i\omega t+ikx} = -i\omega\beta_0 T_0 \mathcal{P} e^{-i\omega t+ikx}$ is applied in the medium, we write the Zwikker and Kosten's equations, in each part of the resonator: tube, neck, and cavity. The aim is to obtain the function $\chi^{-1}(\omega, k)$ as it is indicated in Eq. (2.19b). In the main tube and the cavity, for $\alpha = t, c$, we write

$$-i\omega\frac{\rho_\alpha(\omega)}{S_\alpha}V_\alpha = -\frac{\partial P_\alpha}{\partial x} \tag{2.30a}$$

$$i\omega S_\alpha \chi_\alpha(\omega) P_\alpha + i\omega S_\alpha \left(\chi_\alpha(\omega) - \gamma\chi_0\right)\mathcal{P} = \frac{\partial V_\alpha}{\partial x} \tag{2.30b}$$

The second term in the second equation might not seem to be obvious but follows the very procedure of obtaining (2.19b). In the neck, the equations are written as

$$i\omega\frac{\rho_n(\omega)}{\sigma}V_n = \frac{\partial P_n}{\partial y} \tag{2.31a}$$

$$i\omega\sigma\chi_n(\omega)P_n + i\omega\sigma\left(\chi_n(\omega) - \gamma\chi_0\right)\mathcal{P}\left\langle e^{ikx}\right\rangle_\sigma = \frac{\partial V_n}{\partial y} \tag{2.31b}$$

where the term $\mathcal{P}\langle e^{ikx}\rangle_\sigma$ comes from the averaging of $\dot{Q}$ over the neck cross section. Here also, the second equation might not appear obvious, but follows the procedure of the determination of (2.19b) in nonlocal theory.[28]

As before, the general solution of the non homogeneous equations (2.30) in the right or left part of the tube and the cavity, is written as the sum of the general solution $(P_{\alpha,h}, V_{\alpha,h})$ of the homogeneous equations and a particular solution $(P_{\alpha,p}, V_{\alpha,p})$ of the non homogeneous equations. A general solution of the homogeneous equations

(2.30) is written as Eq. (2.26). The following particular solution can be considered

$$\begin{pmatrix} P_{\alpha,p} \\ V_{\alpha,p} \end{pmatrix} = \begin{pmatrix} B_\alpha \\ C_\alpha \end{pmatrix} \mathcal{P} e^{ikx} \tag{2.32}$$

where B_α and C_α are four constants to be determined. Substituting (2.32) in (2.30) gives the four constants $B_t = \omega^2\rho_t(\chi_t - \gamma\chi_0)/(k^2 - \omega^2\rho_t\chi_t)$, $C_t = \omega k(\chi_t - \gamma\chi_0)\Sigma/(k^2 - \omega^2\rho_t\chi_t)$, $B_c = \omega^2\rho_c(\chi_c - \gamma\chi_0)/(k^2-\omega^2\rho_c\chi_c)$, and $C_c = \omega k(\chi_t-\gamma\chi_0)(L-\Sigma-2L)/(k^2-\omega^2\rho_c\chi_c)$. Thus, the general solution of Eqs. (2.30) can be written as Eqs. (2.28), replacing f with $\mathcal{P}$. The amplitudes A_1, A_2, A_3, A_4, A_7, A_8, A_9, and A_{10} (Fig. 2.5(b)) are to be determined.

As for the tube and the cavity, the general solution of the non homogeneous equations (2.31) in the neck, is written as the sum of the general solution $(P_{n,h}, V_{n,h})$ of the homogeneous equations and a particular solution $(P_{n,p}, V_{n,p})$ of the non homogeneous equations. We can find a particular solution in the following form

$$\begin{pmatrix} P_{n,p} \\ V_{n,p} \end{pmatrix} = \begin{pmatrix} B_n \\ C_n \end{pmatrix} \mathcal{P} \tag{2.33}$$

where B_n and C_n are two constants which will be determined by substituting (2.33) in (2.31):

$B_n = (2/k\sigma)(\gamma\chi_0/\chi_n - 1)\sin(k\sigma/2)$, and $C_n = 0$. To obtain the above expression for B_n, the average $\langle e^{ikx}\rangle_\sigma$ can be easily calculated.[24] Therefore, the general solution of Eq. (2.31) in the neck can be written as

$$\begin{pmatrix} P_n \\ V_n \end{pmatrix} = \begin{pmatrix} 1 \\ Y_n \end{pmatrix} A_5\mathcal{P}e^{ik_n y} + \begin{pmatrix} 1 \\ -Y_c \end{pmatrix} A_6\mathcal{P}e^{-ik_n y} + \begin{pmatrix} B_n \\ 0 \end{pmatrix} \mathcal{P} \tag{2.34}$$

where A_5 and A_6 are amplitude-relating constants to be determined [Fig. 2.5(b)].

As noted previously, in the framework of our modeling, there are 10 relations which are assumed to be verified, allowing to relate the flow rates and pressures at different indicated points in Fig. 2.5(b).

These relations result in 10 equations by which we can compute the amplitudes $A_1, \ldots, A_{10}$.[24] Consequently, all Zwikker and Kosten's fields will be found. After the averages $\langle v \rangle$, $\langle pv \rangle$, and $\langle b \rangle$ are calculated[24] for the actual fields, the expression for $\chi^{-1}(\omega, k)$ will be obtained.

Bloch Wave Modeling

In this section, without using the principles of the nonlocal macroscopic theory but within the same plane wave modeling, we directly seek the macroscopic Bloch wavenumber k_B of the least attenuated wave propagating in the direction of positive x-axis, such that

$$\begin{pmatrix} P_t^{(4)} \\ V_t^{(4)} \end{pmatrix} = e^{ik_B L} \begin{pmatrix} P_t^{(1)} \\ V_t^{(1)} \end{pmatrix} \tag{2.35}$$

with the field constituted of 10 Zwikker and Kosten's slit waves, as illustrated in Fig. 2.5(b), are associated 10 complex amplitudes $A_1, \ldots, A_{10}$. As before, between these 10 amplitudes there are a set of 10 relations; where two of them express the Bloch condition (2.35), and 8 relations are based on the continuity equations. Here, all these relations are homogeneous relations, so that nontrivial solutions will be obtained only if the determinant of the coefficient matrix vanishes. This condition will give the analytical expression for Bloch wavenumber k_B, as follows

$$k_B = -\frac{i}{L} \ln \left(\frac{D}{2} \pm \sqrt{\frac{D^2}{4} - 1} \right) \tag{2.36}$$

where $D = 2\cos k_t L - i(Y_r/Y_t) \sin k_t L$, $Y_r = V_n^{(5)}/P_n^{(5)}$ is the entrance admittance of the resonator (see Eq. (31) in Ref. 24).

2D structure filled with air

For the geometry considered in Fig. 2.5(a), to perform the computations, we have set $L = 1\ cm$, $\Sigma = 0.2\ L$, and $\sigma = 0.015\ L$. The functions $\rho(\omega, k)$ and $\chi^{-1}(\omega, k)$ are first determined within the approximations of our nonlocal modeling. Given these expressions,

we know that according to nonlocal theory the possible wavenumbers in the medium will be the solutions of the dispersion relation (2.20). Solving the equation (2.20) by a Newton-Raphson scheme, we have checked that the obtained expressions for $\rho(\omega, k)$ and $\chi^{-1}(\omega, k)$ are such that a complex solution $k(\omega)$ to (2.20) exists, which is very close to the value $k_B(\omega)$ in (2.36). The frequency dependent effective density $\rho(\omega, k(\omega)) = \rho(\omega)$, and effective bulk modulus $\chi^{-1}(\omega, k(\omega)) = \chi^{-1}(\omega)$, are then obtained by putting $k = k(\omega)$ in the aforementioned excitation terms.

Solving the equation (2.20) by the Newton-Raphson method, we varied frequency step by step, taking as initial value for $k(\omega)$ at a given frequency, the solution value obtained at the preceding frequency. Only for the starting frequency ω_0 in the range of interest, we have chosen the value $k_B(\omega_0)$ with a 10% discrepancy. In order to ascertain the validity of the modeling, we have also performed direct FEM simulations to solve the action-response problems, giving, subsequently, FEM evaluations of the functions $\rho(\omega, k)$ and $\chi^{-1}(\omega, k)$. Based on these functions, the computation of the wavenumber of the least attenuated wave was performed in the same way as just seen, with the only difference that (due to computation time) the initial $k(\omega)$ value at a given frequency was systematically taken to be $k_B(\omega)$ with 10% discrepancy. Finally, FEM evaluations of the frequency dependent effective density $\rho(\omega, k(\omega)) = \rho(\omega)$, and effective bulk modulus $\chi^{-1}(\omega, k(\omega)) = \chi^{-1}(\omega)$, were obtained by putting $k = k(\omega)$ in the aforementioned excitation terms. The FEM computations have been performed using FreeFem++,[53] an open source tool solving partial differential equations. Adaptive meshing was employed. According to all of the calculations, the effective density remains practically constant and, therefore, does not play an important role in the macroscopic dynamics of this material.

We see in Fig. 2.6(a), that the real and imaginary parts of $k(\omega)$ computed by nonlocal theory via Newton's method converge exactly to the real and imaginary parts of k_B which have been computed by a simple Bloch-wave modeling without any use of nonlocal theory. The horizontal axis is the dimensionless frequency $k_0 L/\pi$, where

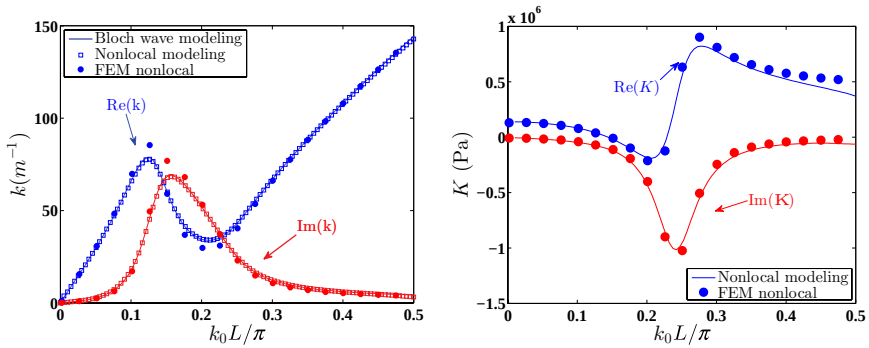

Fig. 2.6. Wavenumber (a) and bulk modulus (b) in terms of a dimensionless frequency, for the 2D structure filled with air. For the wavenumber, results by three calculations are compared: Bloch-wave modeling, nonlocal modeling, and nonlocal theory by FEM.[24]

$k_0 = \omega/c_0$. The results based on the Finite Element Method (FEM) simulations are also in good agreement with those obtained by the Bloch wave modeling and nonlocal modeling. The frequency range has been chosen so that it covers the resonance regime. In the same frequency range, Fig. 2.6(b), shows the real and imaginary parts of $K(\omega) = \phi\chi^{-1}(\omega)$, representing the effective bulk modulus, computed by nonlocal FEM simulations and nonlocal modeling. Here also, we see excellent agreement between the two calculations. We notice the metamaterial behavior demonstrated in the real part of effective bulk modulus which becomes negative in a frequency range within the resonance regime. It is clear that the results by FEM computations based on the exact microscopic equations, can be considered more precise compared with our two modeling results in which we have applied simplifying approximations. As such, the good agreement between FEM results and others, validate the modeling framework. The discrepancies between the results based on the models and FEM simulations can be due in particular, to the fact that the model describes the admittance of the resonator Y_r, without considering the length correction of the neck; what might generate errors in the calculation of the wavenumber.

We observe here the same kind of behavior for the wavenumber and bulk modulus as it has been demonstrated experimentally in Ref. 3 (see Figs. 1 and 2 in that reference) for the case of the 3D material embedded in water. We have observed that removing the thermal effects by decreasing the coefficient of thermal conductivity κ to a value close to zero, would have a negligible effect on the wavenumber and the effective bulk modulus. That is the case also for the second viscosity ζ, associated with losses in the compressional/dilatational motions in the bulk fluid. On the contrary, the material dynamics in terms of the macroscopic wavenumber and bulk modulus is quite sensitive to the values of the shear viscosity η. In a frequency range, for instance, between $k_0L/\pi = 0.1$ and 0.4, a maximum and minimum appear for the real part of the wavenumber. By decreasing the value of the shear viscosity, the maximum becomes sharper and finally diverges as the viscosity tends to zero at the resonance frequency of the ideal fluid $\omega_H = c_0[\sigma/l(L-2l)(L-\Sigma-2l)]^{\frac{1}{2}}$, namely $k_0L/\pi = 0.15$ here; the minimum flattens and a bandgap is created. As a matter of fact, the important feature, here, is the resonant behaviour which induces important values of the velocity in the neck, and thus also important viscous dissipation. Furthermore, at small enough η, at frequencies close but smaller than resonance frequency, the corresponding neck flow becomes predominant and the effective wavelength is drastically reduced, leading to a so-called *slow speed*. However, when the shear viscosity increases, the neck flow adjusts to a smaller value, eventually leading to the disappearance of the *slow speed*. The viscous losses also smooth out the extrema of the real and imaginary parts of the modulus in Fig. 2.6(b). Consequently, a wider frequency range of the negative real part of the bulk modulus is achieved by increasing the viscous losses. The thermal boundary layers close to the cavity walls, where the fluid bulk modulus passes from adiabatic to isothermal value, mainly bring a small correction to the cavity spring constant (the cavity dimension is much larger than the boundary layer thickness $\delta_t = (2\kappa/\rho_0 c_p \omega)^{\frac{1}{2}}$). Therefore, their presence do not affect much the effective bulk modulus.

As explained before, the dynamics of the material will be very sensitive to the width of the neck, where a considerable part of the viscous losses take place. In our case (see values of the parameters in Fig. 2.5), between the frequencies $k_0L/\pi = 0.1$ and 0.4, the ratio of the viscous boundary layer thickness $\delta_v = (2\eta/\rho_0\omega)^{\frac{1}{2}}$ to the width of the neck, insensibly changes from 0.35 to 0.39. We observed that, in general, to maintain the similar behavior of the wavenumber and modulus, this ratio should remain in the same order, regardless of changing the scale of the material or the saturating fluid. Here, well above the resonance, at $k_0L/\pi = 0.5$, we can check that the effective wavelength in the material λ_{eff} is comparable to that in air λ_0: $\lambda_{eff}/L \sim 5$, and $\lambda_0/L = 4$. At the resonance frequency $k_0L/\pi = 0.15$, we find that $\lambda_{eff}/L \sim 8$. Roughly, this is a reduction by a factor of two of the wavelength in air ($\lambda_0/L \sim 13.33$), and an illustration of the mentioned trend of a *slow speed* close to the resonance. Although this structure represents a subwavelength material, and therefore, can be regarded in the large wavelength limit $\lambda_{eff} \gg L$, the local theory based on the two-scale homogenization at order zero does not predict correctly the acoustics, ignoring the resonance behavior. The origin of the failure is the presence of widely different length scales, allowing for resonances.

The same modeling framework has been used to study the case of 3D materials.[24] It has been noted that,[24] if the structure with the same geometrical parameters is embedded in water, there would be less loss as the the viscous boundrary layer thickness is smaller compared with that of air. To keep the same dynamic behavior with water as with air, it would be necessary to very significantly decrease the width of the neck; at this point it should be in mind that the complicated effect of nonlinearities would certainly have to be taken into account. Furthermore the thermal effects in water are not important. The general thermodynamic identity $\gamma - 1 = \beta_0^2 T_0/\rho_0 c_p$, shows that the deviation of $\gamma \equiv c_p/c_v$ from unity, is a second order effect on the thermal expansion coefficient β_0. For a liquid, like water, β_0 is very small; what implies that γ is practically 1. In this case, adiabatic bulk modulus $\chi_{0(adiab)}^{-1}$ and isothermal bulk modulus $\chi_{0(isoth)}^{-1}$

are very close, since in general, $\chi^{-1}_{0(adiab)} = \gamma\chi^{-1}_{0(isoth)}$. Therefore, thermal exchanges have practically no effects.

2.2.4. *Sound focusing and negative index acoustic metamaterials*

The first experimental demonstration of focusing ultrasound waves through a flat acoustic metamaterial lens composed of a planar network of subwavelength Helmholtz resonators has been presented in Ref. 13. A tight focus of half-wavelength in width at 60.5 kHz by imaging a point source has been observed. This result was in excellent agreement with the numerical simulation by transmission line model in which the effective mass density and compressibility has been derived.

Negative Refractive Index Lens

The refractive index is a fundamental parameter describing the interaction between waves and material. In late 1960s, Veselago[54] first considered the theoretical possibility for a medium having simultaneous negative permittivity and negative permeability. When $\varepsilon(\omega) < 0$, $\mu(\omega) < 0$ at certain frequency, the refractive index is $n = -\sqrt{\varepsilon\mu}$ and the negative sign is taken to satisfy causality. When light passes from a positive ($n > 0$) to a negative ($n < 0$) medium, Snell's law implies that the angle of refraction is negative, showing the refracted ray emerges on the same side of the normal as the incident ray. In 2000, Pendry[55] proposed that a thin slab of metamaterial with negative refractive index could make a *perfect lens* without any loss of details. A conventional lens cannot focus light onto an area smaller than a square wavelength due to the diffraction limit. The reason for this limit is that the evanescent waves which carry the subwavelength details of the object are exponentially decaying, leading to the loss of those fine features in the image. However, utilizing negative refractive index material, a *perfect lens* can focus propagation waves and also amplify evanescent waves to generate subwavelength imaging.

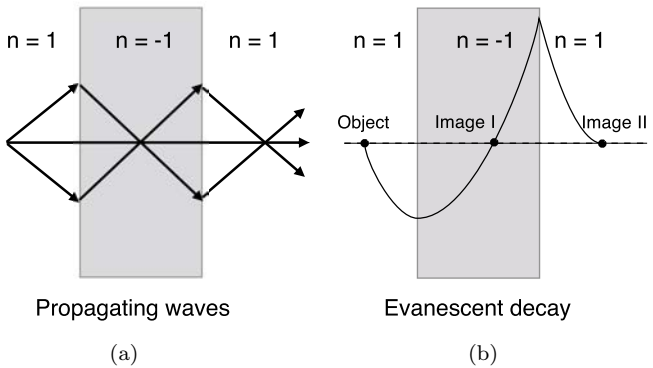

Fig. 2.7. A flat lens brings all the diverging rays from an object into two focused images (a). The NI medium can enhance the evanescent waves across the lens, so the amplitude of the evanescent waves are identical at the object and the image planes (b).

As shown in Fig. 2.7, negative refraction allows a flat slab lens of negative index (NI) to focus all the diverging light rays from an object into two images: one inside the slab and the other one outside the slab. The evanescent waves have been enhanced across the lens and decay again after emerging from the negative index lens. Therefore the amplitude at the two image planes reaches their original level. At the same time, the propagating waves pass through the negative index lens with a reversed phase front, leading to zero phase change at the image planes. By completely recovering both propagating and evanescent waves in phase and amplitude, a perfect image is obtained.

An approximation of the *perfect lens* called as *super lens* was built in optical frequency range under near-field condition. In the near field, since the electric and magnetic components are decoupled, the *super lens* only needs negative dielectric permittivity for one polarization light. The optical superlensing effect on the scale of 60 nm ($\lambda/6$) was observed by excitation of surface plasmons[56] through the metal/dielectric layer structure. The sub-diffraction-limited image was recorded by optical lithography at 365 nm wavelength. In microwave frequency, subwavelength focusing was realized by different groups. An example of subwavelength focusing in

microwave frequency has been realized using a planar transmission-line structure.[57] The negative index lens is a planar slab consisting of a grid of printed metallic strips over a ground plane, loaded with series capacitors and shunt inductors. In the experiment, the loaded grid is sandwiched between two unloaded printed grids that act as effective homogeneous media with a positive refractive index.

Sound Focusing by Acoustic Transmission Line Network

Figure 2.8 shows the experimental setup to study the focusing phenomena of the acoustic metamaterial. To prepare the sample, we machined a 2D array of periodically connected subwavelength Helmholtz resonators in an aluminum plate and the resonators are filled with water. As shown in previous work,[58–60] a main transmission channel with recurrent side branches, which are closed at the

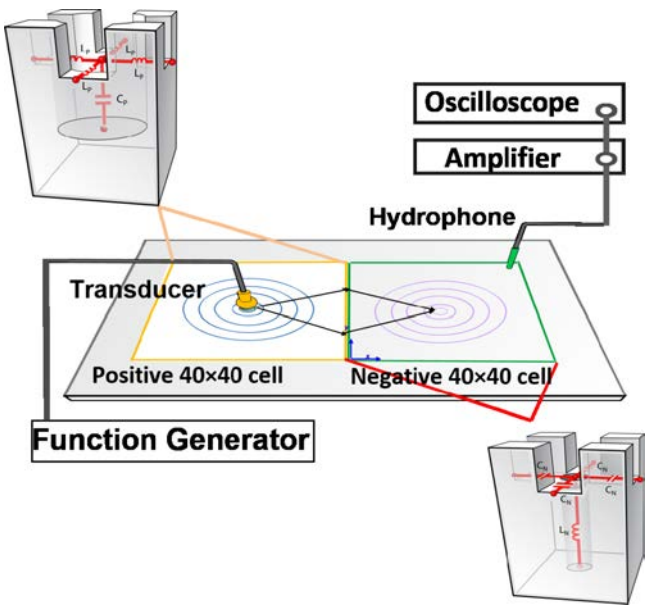

Fig. 2.8. Schematic showing the experimental setup. The sample with PI-NI interface is composed of an array of different designed Helmholtz resonators machined from an aluminum plate. Unit cells of each half part and the corresponding inductor-capacitor circuit analogy are shown in the insets.[13]

outer end, is analogous to a circuit of a series of inductors with shunt capacitors. On the other hand, when the side tubes inserted in the main channel are open on the outer end, the acoustic system can be described by a lumped network of a series of capacitors with shunt inductors. The left and right half parts in the sample are 2D periodic versions of those different types of topology, respectively. One unit cell from each half part is enlarged and shown in the two insets, respectively.

The left half part is composed of a 2D array (40×40) of large cavities connected with main channels. The volume of the cavity is around 10 times that of one section of the channels. Such an acoustic system is analogous to an inductor-capacitor circuit as shown in the inset of Fig. 2.8 with the channels acting as a series of inductors (L_P) and the cavity providing the stiffness element as capacitors (C_P). The periodicity (3.175 mm) of the sample is one-eighth of the wavelength at around 60 kHz frequency range. Given this value, the lumped circuit model is a valid approximation for the distributed acoustic system with only 10% error.[62] Following the approach of EM circuit analysis (see also Section 2.2.1),[27,57,61] the effective density and compressibility of this network can be expressed in the form as $\rho_P = L_P S_P/d_P$, $\chi_P = C_P/S_P d_P$, where d_P is the periodicity and S_P is the cross section area of the channels. Both effective density and compressibility are positive. Effective relative acoustic refractive index n_P can be determined by $n_P = c_0\sqrt{L_P C_P}/d_P$ where c_0 is the speed of sound in water. We call this half part the effective positive index (PI) medium. Such an acoustic system is described as a lumped network with a series of capacitors (C_N) for the main channel part and a shunt inductor (L_N) due to the orifice. The periodicity is the same as that in the left part, so the effective mass density and compressibility can be similarly estimated as $\rho_N = -S_N/(\omega^2 C_N d_N)$, $\chi_N = -1/(\omega^2 L_N d_N S_N)$ where d_N is periodicity and S_N is the cross section area of connecting channels. Both parameters are negative. The refractive index $n_N = c_0/c(\omega) = -c_0/(\omega^2 d_N\sqrt{L_N C_N})$ is negative. Therefore, this material acts as a medium exhibiting NI of refraction. The two half parts are designed with effective indices of

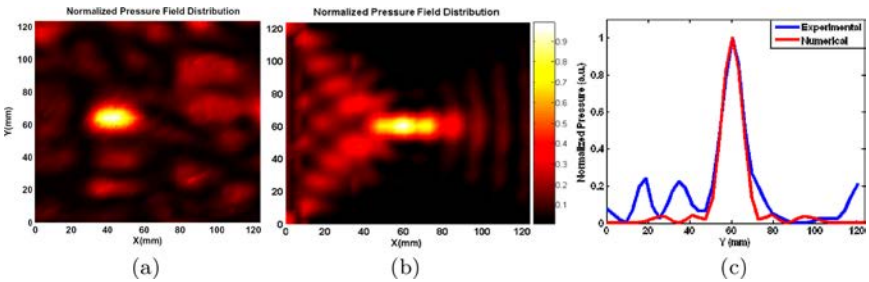

Fig. 2.9. Pseudocolor map of the normalized pressure field distribution at 60.5 kHz. Measured (a) and simulated (b) field map of the acoustic NI metamaterial and line plot of pressure field across the focal plane parallel to interface (c).[13]

equal and opposite value and matched impedance $\sqrt{\rho/\chi}$ at the design frequency 60.5 kHz.

In the experiments, the pressure field through this PI-NI interface has been measured to confirm the focusing in this material. Comparison of Figs. 2.9(a) and 2.9(b) shows that the field plots found through simulation, by circuit simulator SPICE, are in remarkable agreement with the experimental results.

In Fig. 2.9(c), the measured data shown by the blue line is shifted to the left by 3.175 mm for comparison purposes. The comparison demonstrates a very good match in the focus width between the measurement and the numerical simulation. This analysis predicts that the negative refractive index approaches -1 relative to the PI part at 60.5 kHz. In order to achieve high-quality focus imaging, the ratio of the refractive index should be -1 at the PI-NI interface. Only when the index is matched, based on ray acoustics, the angle of refraction equals the angle of incidence for each ray such that all rays can be brought to the same focal spot in the NI part. However, the refractive index is not exactly matched in the experiment. This discrepancy is related to the loss as well as variation in the inductors and capacitors from their designed values due to machining tolerance. It has been noted that single PI-NI interface does not allow enough growth of evanescent fields to achieve subdiffraction focusing[61] while sandwich structure (two PI-NI interfaces) offers a better chance to overcome the diffraction limit.[57]

The emission of a point source at kilohertz frequency which was brought to a focus through the PI-NI interface because of the negative refraction in this ultrasonic metamaterial, has been expected to be a step toward a novel acoustic imaging lens. The resolution of 0.5 wavelength was recorded by focusing the acoustic field of a point source. This is not subdiffraction imaging, but among the best achievable passive acoustic imaging elements. The unit cell of the acoustic network is only one-eighth of the operating wavelength, making the lens a compact size. Compared with conventional lenses, the flat thin slab lens has advantages in that there is no need to manufacture the shapes of spherical curvatures and the focus position is insensitive to the offset of source along the axis. Also, this negative-index lens offers tunable focal length at different frequencies.[13]

2.2.5. *Extraordinary focusing of sound above Helmholtz resonator array*

Recently, Lemoult *et al.*[63] used time reversal to focus sound above an array of soda cans into a spot much smaller than the acoustic wave length in air. However, the time reversal may not be necessary to achieve the extraordinary focusing in such system. In this section, we will experimentally demonstrate the extraordinary focusing above an soda can array using monochromatic sound excitation. We will also explain the experimental observations based on an analytical effective-medium model as well as finite-element calculations.[25]

2.2.5.1. *Experimental configuration and results*

As shown in Fig 2.10(a), we arranged 37 empty soda cans in a hexagonal array. Six commercial speakers, which were continuously driven at a given frequency, were placed symmetrically around the array. In the experiment, the Coca-Cola cans have a volume of 350 cm^3 and an opening area of 4 cm^2 similar to those used by Lemoult *et al.*,[63] with the fundamental Helmholtz resonance at 420 Hz. A microphone mounted on a translation stage was suspended at a height of 12 ± 2 mm above the top of the cans to collect acoustic intensity

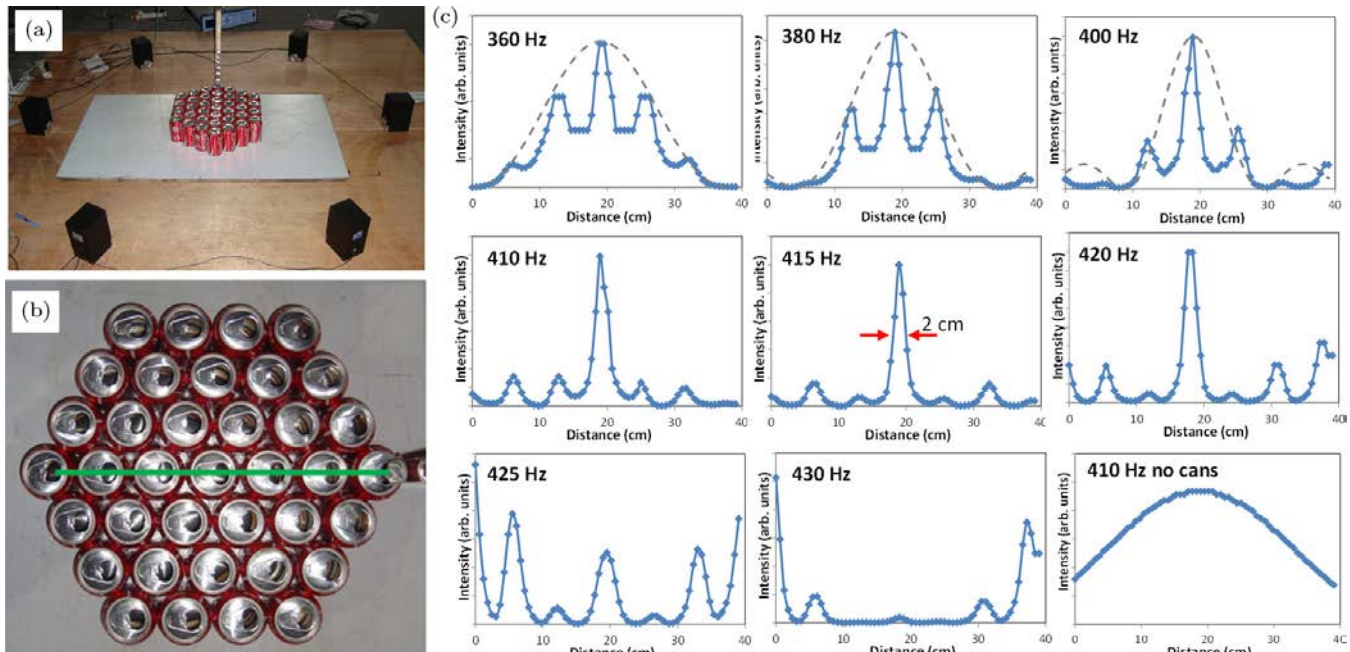

Fig. 2.10. (a) Experimental arrangement inside the anechoic room; (b) top view of the array with the scan line shown; (c) Acoustic intensity profiles along the diameter of the array at different frequencies. The bottom right panel shows an intensity profile measured without soda cans. Symbols are experimental points, connecting lines are guides to the eye. Dashed lines are Bessel function envelopes.[25]

distribution. The experimental results of the acoustic intensity profiles at different frequencies as well as a reference profile measured without cans are plotted in Fig. 2.10(b). Without the soda can array, a focal spot with a FWHM (full width at half maximum) of 31 cm at 410 Hz is observed, which is around 0.37 of the wavelength. With the soda can array, the focal spot at the center of the array gets progressively smaller as the resonant frequency is approached from below, becoming as narrow as 2 cm, or about $\lambda/40$, at 415 Hz. Above the Helmholtz resonance frequency, the intensity profile changes dramatically with maxima at the edges of the array and attenuation towards the center.

2.2.5.2. *Theoretical modeling*

In the effective medium approach, the acoustic wavelength is assumed to be much greater than the average distance between the resonators. The resonators can be modeled as mass-on-a-spring harmonic oscillators with pistons of mass M attached to springs with spring constant K as shown in Fig. 2.11(a). The resonators are regularly distributed in two dimensional plane with the average fractional piston area F.

For a Helmholtz resonator with a zero neck length, the effective mass is estimated as $(16/3)\pi^{-3/2}\rho_0 A^{3/2}$, where A is the opening area and ρ_0 is the density of air, whereas the spring constant K is given by $\rho_0 c^2 A^2/V$, where c is the speed of sound and V is the volume of the resonator.[64] For our soda cans, this model yields an effective mass of 9.23 mg and a spring constant of 64.8 N/m, resulting in a resonance frequency $\omega_0/2\pi = 422$ Hz.

The vertical position of a piston Z is obeying the equation of motion:

$$\ddot{Z} = -\omega_0^2 Z - \frac{pA}{M}, \tag{2.37}$$

where p is a deviation of the pressure above the piston from the equilibrium value and A is the area of the piston. In the case of long wavelength assumption, the average displacement of the boundary can be written as $u_z = FZ$. This leads to an effective boundary condition relating the average displacement and pressure at the boundary

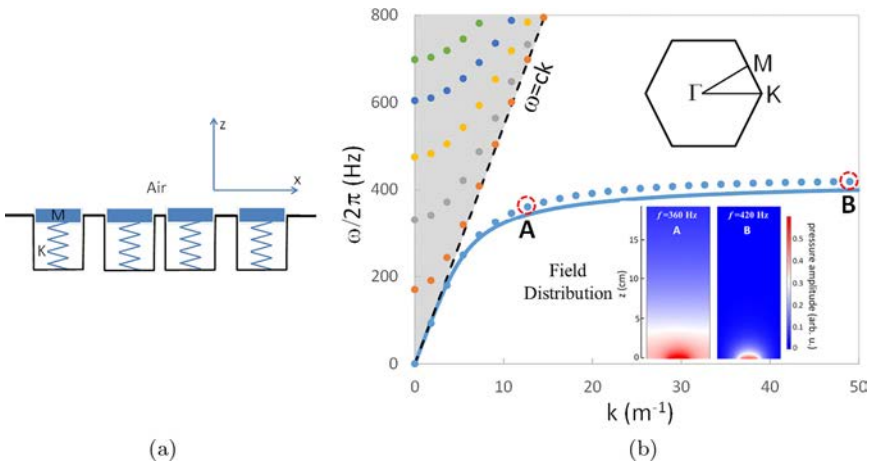

Fig. 2.11. (a) The model system. (b) Dispersion of acoustic waves propagating above the hexagonal array of soda cans calculated by FE (symbols) along the ΓK direction of the reciprocal lattice vs. the effective medium calculation (solid line). Shaded area represents the continuum of bulk modes in the semi-infinite space whereas FE calculations yield discrete modes due to the finite height of the simulation domain. The inserts are distributions of the sound pressure amplitude in the guided mode above a soda can for points A and B of the dispersion curve.[25]

$z = 0$,

$$\ddot{u_z} + \omega_0^2 u_z = -\frac{pFA}{M}, \tag{2.38}$$

which replaces the boundary condition of zero displacement at the rigid boundary in the absence of resonators. By assuming a harmonic wave propagating along the x direction, $\phi = \tilde{\phi}(z) \exp(i\omega t - ikx)$, we can achieve the following equation of motion:

$$\frac{\partial^2 \tilde{\phi}}{\partial z^2} = \left(k^2 - \frac{\omega^2}{c^2}\right) \tilde{\phi}, \tag{2.39}$$

and finally get a dispersion relation for ω and k,

$$\left(k^2 - \frac{\omega^2}{c^2}\right)^{1/2} (\omega_0^2 - \omega^2) = \frac{\omega^2 FA}{M}. \tag{2.40}$$

The dispersion relation is plotted in Fig. 2.11(b) (solid line) for $\rho_0 = 1.23$ kg/m^3, $c = 343$ m/s, $F = 0.106$ (calculated for dense

hexagonal packing of the cans). In the limit of small k the dispersion approaches that of the bulk wave in air, $\omega = ck$, whereas in the opposite limit of large k the frequency asymptotically approaches the resonance frequency ω_0. For a more accurate description of the wave propagation above a hexagonal lattice of soda cans, we use finite element (FE) calculations.

The acoustic module in COMSOL Multiphysics was applied to calculate the dispersion relation of soda cans arranged in a hexagonal lattice. Soda cans were modeled as cylinders with rigid walls of 11.5 cm in height and 6.6 cm in diameter. The opening in the model was circular and centered at the axis of the cylinder, with the same area of 4 cm^2 as the opening of a real can. Due to the computational resource limitation, the height of the simulation domain was set as 1 m, with rigid wall boundary conditions at the "ceiling". Floquet periodic boundary conditions were applied in order to find acoustic eigenmodes of an infinite 2D hexagonal lattice. The calculated dispersion relation along the ΓK direction of the reciprocal lattice is plotted in Fig. 2.11 (symbols). Discrete modes in the shaded area above the sound line $\omega = ck$ are due to a finite height of the simulation domain. For a semi-infinite half space, the shaded area should be filled by a continuum of bulk waves propagating at oblique angles to the floor. The mode below the sound line is guided by the can array, and its dispersion is close to what the simple effective medium theory has predicted.

In conclusion, we have demonstrated that focusing of sound in a metamaterial formed by a 2D array of soda cans results in an increasingly narrow intensity peak as the acoustic frequency approaches the Helmholtz resonance from below. The observed phenomenon results from the small acoustic wavelength in the metamaterial in combination with a near-field effect, i.e., the localization of the acoustic intensity at the opening of a can at frequencies close to the resonance. Furthermore, we found that the acoustic wave propagating along the Helmholtz resonator array is a guided mode becoming increasingly confined to the array as its frequency approaches the Helmholtz resonance from below.

2.3. Acoustic Transformation and Its Application

As we could see earlier, acoustics and electromagnetism have been brought together through different analogies derived from high similarities in their formalisms, despite deep differences in their physical nature. How coordinate transformation was used in both fields, does not make an exception to that rule. In 2006, Pendry *et al.*[16] showed that one could manipulate at will[a] the wave propagation in the framework of a relatively easy formalism -transformation optics, the coordinate transformation in optics- in comparison with the offered possibilities. Soon, the concept was transposed to acoustics.

Among the foreseen applications, the invisibility cloak has been the subject of first experimental studies in late 2006.[20] It was followed later by the acoustic ("inaudible") cloak, first realized in 2011 for acoustic waves[50] and in 2012 for elastic waves.[66] In this section, we start by a brief summary of the recent rebirth of coordinate transformation in optics and acoustics, with an emphasis on the "inaudible" acoustic cloak.[50] Then, we show how coordinate transformation can be broadly applied to different physics and lead for example to surface wave cloaking. Finally, we show that the concept of coordinate transformation can be applied more generally, allowing for example the design of a complementary material meant to remove the aberrations resulting from the transmission of an acoustic wave through any arbitrary heterogeneous medium.

2.3.1. *Transformation acoustics*

2.3.1.1. *Coordinate transformations and invisibilty*

The work by Pendry *et al.* that was published in 2006, is in fact based on the conclusions of an article published 10 years earlier. In 1996, Ward and Pendry showed that Maxwell's equations are invariant under any arbitrary transformation of coordinates.[65] In other words, after the coordinate transformation, their form is the same as the one

[a]The control of wave propagation relies by spatially controlling the material parameters ϵ and μ.

they have in the Cartesian mesh. The only difference is that if we start with an isotropic material for which ϵ and μ are scalar, after the coordinate transformation, we generally end up with anisotropic and heterogeneous material for which ϵ and μ are represented by tensors.

This form invariance can be used in a smart way. Indeed, chosen in a suitable manner, the coordinate transformation makes it possible to exclude the field from any arbitrary surface (2D) or volume (3D). Furthermore, it can be chosen so that the field lines are reformed on each side of the prohibited area, thus making this space invisible to any observer or listener.

In view of the invisibility cloak, the first coordinate transformation scheme that was historically provided, was to exclude waves from a sphere.[16] As we discuss later the two dimensional case, we present here one coordinate transformation which allows us to exclude the field from a disk surface:

$$\begin{aligned} r' &= R_1 + r(R_2 - R_1)/R_2 \\ \theta' &= \theta \\ z' &= z \end{aligned} \tag{2.41}$$

This coordinate transformation makes the region of space that is comprised in the circle of radius R_1 inaccessible, as it moves the points of that region to the region defined by $R_1 < r < 2R_1 - {R_1}^2/R_2$. Meantime, the space that was originally defined by $R_1 < r < R_2$, is squished in the region defined by $2R_1 - {R_1}^2/R_2 < r < R_2$. Space beyond R_2 remains unchanged. For the rays, whether they are of light or sound, the trajectories that initially borrow straight lines within the region $r < R_2$ become more or less severely curved in order to avoid the forbidden region (see Fig. 2.12).

This apparent simplicity has a cost, which is reflected in the way the parameters of the medium are changed by the coordinate transformation. Their calculation involves the Jacobian matrix of the latter, and the parameters of the non-deformed/homogeneous medium. As we have mentioned earlier, the new material parameters generally depend on the position but also on the direction.

Finally, we note that in the invisibility cloak, the trajectories are curved, and therefore they are longer than the straight trajectories

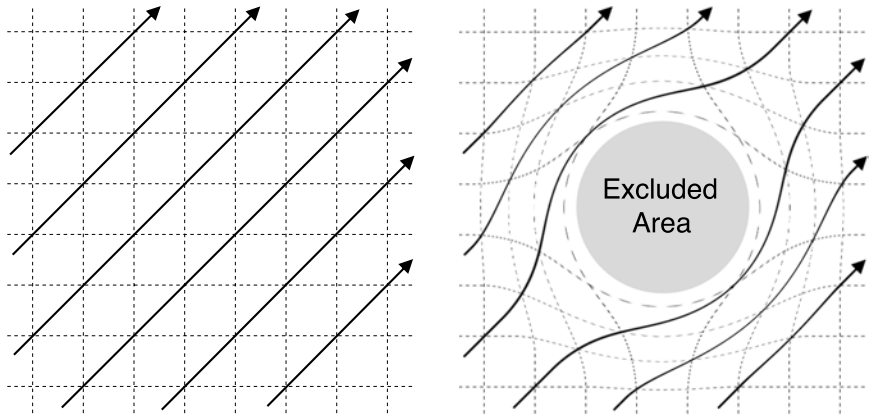

Fig. 2.12. Starting with a homogeneous configuration (a), the medium is deformed to exclude rays — of light or sound — (thick arrow lines) from the desired area (b). The coordinate transformation is *recorded* by comparing the ray arrows on both side, and applied to the equations to find the value of the new material parameters (or metamaterial).

in the medium surrounding the cape. For the wavefront to emerge non-deformed after it went through the cape, it is necessary that the speed of the wave is higher in the cloaking device than in the surrounding material.

This raises some issues in optics, where it is hard to fabricate a medium in which light propagates faster than in a medium of reference such as air.[b] On the contrary, in acoustics, there exists many media in which sound travels faster than in reference media such as water or air.

2.3.1.2. *From transformation optics to transformation acoustics*

In acoustics, the first study on coordinate transformation coincides with an article from Milton *et al.* which shows that the equation of

[b]In the cloaking device, it is the phase speed c_ϕ that is higher than the speed of wave outside the cloaking device. The group velocity c_g is given by the relation $c_g = {c_0}^2/c_\phi$ which ensures that it is always lower than c_0.

elasto-dynamic does not generally remain unchanged by coordinate transformation.[67] From this observation, attempts to apply coordinate transformation to the equation of acoustic, mainly focused on finding forms of the equation of acoustic that are similar to the form of Maxwell's equations.

Steven Cummer and David Schurig[68] consider the propagation of acoustic wave in a z-invariant 2D inviscid homogeneous fluid with anisotropic density $\rho = [\rho_r, \rho_\phi]$ and bulk modulus K_0.[c] Assuming time harmonic wave ($\exp(+j\omega t)$ convention), they write the equations for the conservation of momentum and mass in cylindrical coordinates as follows:

$$j\omega\rho_\phi v_\phi = -\frac{1}{r}\frac{\partial p}{\partial \phi}, \tag{2.42}$$

$$j\omega\rho_r v_r = -\frac{\partial p}{\partial r}, \tag{2.43}$$

$$j\omega K^{-1} p = -\frac{1}{r}\frac{\partial (r v_r)}{\partial r} - \frac{1}{r}\frac{\partial v_\phi}{\partial \phi}. \tag{2.44}$$

where p is the pressure and $\mathbf{v} = (v_r, v_\phi)$ is the particle velocity. At the same time, Cummer and Schurig notice that the z-invariant 2D Maxwell equations for transverse electric (TE) polarization, can be written in the following form:

$$j\omega\mu_r(-H_r) = -\frac{1}{r}\frac{\partial(-E_z)}{\partial \phi}, \tag{2.45}$$

$$j\omega\mu_\phi H_\phi = -\frac{\partial(-E_z)}{\partial r}, \tag{2.46}$$

$$j\omega\epsilon_z(-E_z) = -\frac{1}{r}\frac{\partial(r H_\phi)}{\partial r} - \frac{1}{r}\frac{\partial(-H_r)}{\partial \phi}. \tag{2.47}$$

Comparing these three equations to the equations of acoustics (2.42–2.44), they find that these two sets of equations are similar under the

[c]This medium is a transversely isotropic fluid.

following substitution:

$$[p, v_r, v_\phi, \rho_r, \rho_\phi, K^{-1}] \leftrightarrow [-E_z, H_\phi, -H_r, \mu_\phi, \mu_r, \epsilon_z] \tag{2.48}$$

This analogy between the time harmonic acoustic equations and Maxwell equations also preserves boundary conditions. Indeed, the pressure and the normal velocity component are continuous at a fluid-fluid interface, as the vertical component of the electric field and the tangential component of the magnetic field are at an electromagnetic material interface.

Following analogy (2.48) and applying the coordinate transformation corresponding to the equations (2.41) imposes the value of the material parameters K and ρ, inside the cloaking shell ($R_1 < r < R_2$), as follow:

$$\frac{\rho_r}{\rho_0} = \frac{r}{r - R_1} \tag{2.49}$$

$$\frac{\rho_\phi}{\rho_0} = \frac{r - R_1}{r} \tag{2.50}$$

$$\frac{K^{-1}}{{K_0}^{-1}} = \left(\frac{R_2}{R_2 - R_1}\right)^2 \frac{r - R_1}{r}. \tag{2.51}$$

Within the cloaking device ($R_1 < r < R_2$), the effective material parameters continuously change. In the limit $r \to R_1$, $\rho_r \to +\infty$, $\rho_\phi \to 0$ and $K \to +\infty$. Note here that there is no restriction on the values of K and ρ in the cloaked area, i.e., in the region $r < R_1$.

Other studies have shown such analogy between electromagnetism and acoustic equations. In particular Chen and Chan have shown that, in 3D, the acoustic equation in a heterogeneous fluid and the electrical conductivity equation have equivalent forms, therefore allowing to use coordinate transformation in order to guide acoustic wave in 3D-fluid.[69]

2.3.2. *Broadband acoustic cloak for ultrasound*

First numerical simulations are reported by Cummer and Schurig in Ref. 68 where a cylindrical cloaking shell is simulated based on

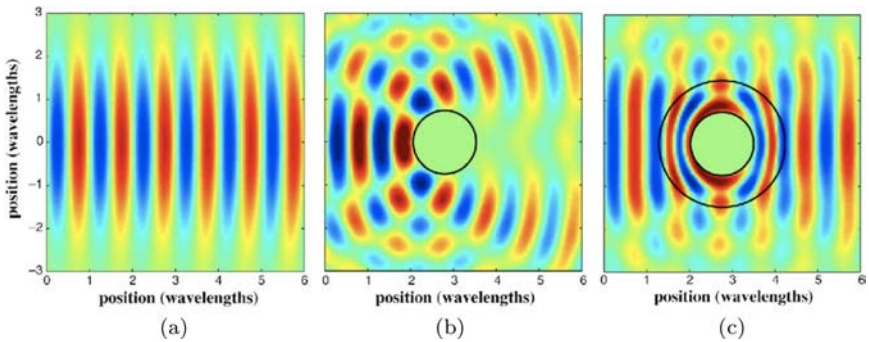

Fig. 2.13. Numerical simulation of an acoustic cloak from Ref. 68. (a) An acoustic beam is propagating in a homogeneous medium. (b) The acoustic beam is scattered by a cylindrical scatterer ($\varnothing = 0.7\lambda$). (c) The scatterer is surrounded by the acoustic cloaking shell.

analogy (2.48). Three configurations are compared: (a) an acoustic beam is sent in a homogeneous medium, (b) the beam encounters an incompressible cylindrical scatterer and (c) the beam encounters the cylindrical cloaking shell (0.75 wavelength thick) surrounding the scatterers. As expected, in configuration (b), the incompressible cylinder is responsible for large scattering and a shadow behind the cylinder. The latter disappears in configuration (c). Indeed, in the forward direction, the wavefront is reformed and retrieves with fairly good agreement the shape of the wavefront in configuration (a), as if there was no scatterer. As in Ref. 67, the difficulties going from the numerical study to the experimental proof are raised. Indeed, in nature, no material has the features of the cloak, namely, a continuous variation of the parameters of the medium along the radius of the cloaking shell, and an anisotropic density.

This challenge was met by Zhang et al. to whom we owe the first experimental realization of the acoustic inaudible cloak[50] for 2D acoustic wave in water. As shown in Fig. 2.14, the cloaking shell is divided in several concentric rings, each one being characterized by a particular set of acoustic material parameters.[d] The rings themselves

[d]As a reminder, ρ_r, ρ_θ and K all vary along r.

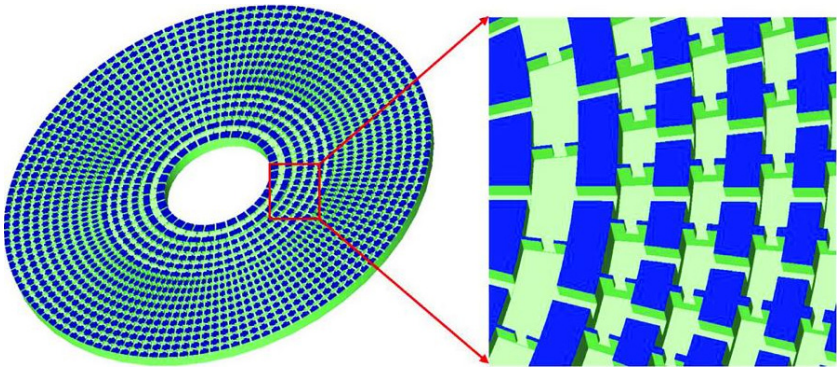

Fig. 2.14. Schematic of cloaking shell for 2D acoustic wave in water, from.[50] The aluminum cloak is devided into 16 concentric rings, with inner and the outer radii of the cloak equal to 13.5 mm and 54.1 mm.

are divided in small cells arranged in a circular array. Each cell is made of a large cavity surrounded by four narrow channels, communicating with the four neighboring cells (two on the same ring and two on the two surrounding rings). The cavity behaves as acoustic capacitor whereas the channels act as serial inductors as seen in Section 2.2.1. Around the central working frequency (60 kHz), each cell is only of the order of one tenth of the wavelength.

Figures 2.15(a–c) shows experimental pressure field mappings resulting from the scattering of an acoustic wave by a bare steel cylinder in water at three different frequencies (60 kHz, 52 kHz and 60 kHz). It is compared to the pressure field mappings when the steel cylinder is surrounded by the acoustic cloak (Figs. 2.15(d–f)). Although the acoustic cloak central frequency is 60 kHz (Figs. 2.15(a) and (d)), the acoustic cloak shows also great results at 52 kHz (Figs. 2.15(b) and (e)) and 64 kHz (Figs. 2.15(c) and (f)). Indeed, the steel cylinder shade is almost completely removed once it is surrounded by the acoustic cloak.

2.3.3. *Molding water, acoustic and electromagnetic waves with a single cloak*

In the most of invisibility cloaking demonstrations, the carefully designed artificial structure can be valid only for one physical

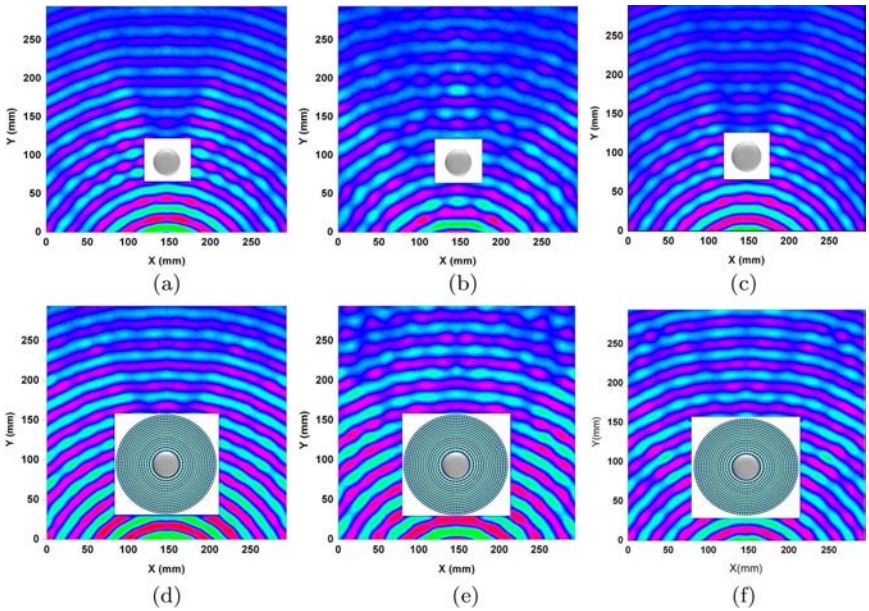

Fig. 2.15. Measured pressure field mappings of the bare cylinder and the cloaked steel cylinder illuminated with a point ultrasound source. The cloak lies in the center of a water tank and surrounds the steel cylinder. The scattering field patterns of the bare cylinder at (a) 60 kHz (b) 52 kHz, and (c) 64 kHz. The pseudo-color map in the immediate environment of the cloaked steel cylinder at (d) 60 kHz (e) 52 kHz, and (f) 64 kHz.[50]

variable, e.g., electromagnetic wave,[20,70–73] acoustic wave,[50,68,69,74,75] elastic wave,[66,76,77] and heat flux,[78–80] etc. In this section, we will introduce a cylindrical cloak which can work equally for linear surface liquid wave, acoustic wave, and electromagnetic wave.[74,81] This structured cloak behaves like a surface liquid wave cloak with an effective anisotropic shear viscosity, an acoustic cloak with an effective anisotropic density, and an electromagnetic cloak with an effective anisotropic permittivity, respectively. The effective anisotropic effect parameters are proceeded with mathematical approach of homogenization,[82,83] which amounts to replacing a structured material by an effective medium that captures the essential wave phenomena for wave with wavelength large compared to the typical heterogeneity

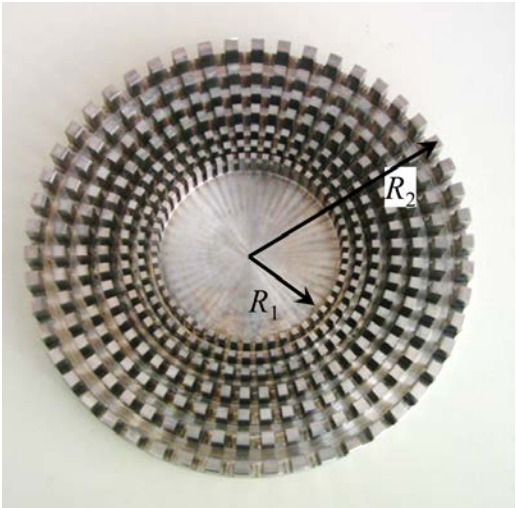

Fig. 2.16. Photo of the structured cloak. 100 rigid sectors are evenly machined in a metallic ring of inner radius $R_1 = 41$ mm and outer radius $R_2 = 100$ mm.[74]

size. We also numerically and experimentally demonstrate the performance of the cylindrical cloak in these three kinds of waves.

2.3.3.1. *Sample configuration*

The invisibility cloak as shown in Fig. 2.16 is manufactured in aluminum using classical numerically controlled machine tools. The outer and inner radii are $R_2 = 100$ mm and $R_1 = 41$ mm, respectively. The cloak is first divided into 14 layers with the layer thickness as the function of r as $(\frac{R_2(r-R_1)}{r(R_2-R_1)})^2$. One layer in two is further divided into 100 identical angular sectors along the azimuthal direction as shown in the figure, and there are seven rows of rods along the radius.

2.3.3.2. *Theoretical and numerical approaches*

For the the surface of a linear fluid medium, the conservation of momentum leads to the Navier-Stokes equations:

$$\rho_0 \left(\frac{\partial}{\partial t} + \mathbf{v} \cdot \nabla \right) \mathbf{v} - \eta \nabla^2 \mathbf{v} = -\nabla p + \rho \mathbf{g} \tag{2.52}$$

where $\mathbf{v}$ is the velocity field, $\eta\nabla^2\mathbf{v}$ accounts for the fluid's viscosity, p the fluid pressure, ρ_0 is density and $\mathbf{g}$ the vector of gravity force. Note that $\mathbf{g} = -g\mathbf{e}_3$, where g denotes the acceleration caused by gravity and $\mathbf{e}_3$ a vertical unit vector. It is noted that $\eta\nabla^2\mathbf{v}$ can be neglected outside the cloak region due to the fairly low viscosity of the surrounding fluid. In addition, the fluid should be also incompressible (divergence free), irrotational (curl free), and undergo only small fluctuations around a mean vertical position. Therefore, the deduced vertical displacement of the fluid for the harmonic oscillation can satisfy with Helmholtz's equation.[84] By solving the Eq. (2.52) for the cloak region, we can achieve an anisotropic matrix of viscosity whose nontrivial part (transverse shear) is:

$$[\eta_{hom}] = \frac{1}{A(Y^\star)} \begin{pmatrix} A(Y^\star) - \psi_{rr} & \psi_{r\theta} \\ \psi_{\theta r} & A(Y^\star) - \psi_{\theta\theta} \end{pmatrix} \tag{2.53}$$

Here, $A(Y^\star)$ denotes the area of the region $Y^\star$ surrounding a rigid inclusion (subject to Neumann boundary conditions) in an elementary cell Y of the periodic array, and ψ_{ij} represent corrective terms, which is related to periodic hydrostatic fields, as shown in Fig. 2.17(a). For simplification, in our sample, we can introduce some variation in the radial length of sectors for which it seems reasonable to assume that the improved cloak is characterized by an effective anisotropic fluid whose shear viscosity (a diagonal matrix in polar basis) is

$$\eta'_{rr} = \left(\frac{R_2(r - R_1)}{r(R_2 - R_1)}\right)^2, \quad \eta'_{\theta\theta} = \left(\frac{R_2}{R_2 - R_1}\right)^2 \tag{2.54}$$

where R_1 and R_2 are the inner and outer radii of the ring, respectively. Importantly, the effective fluid's density is the same as the fluid density, which does not play any prominent role. These parameters were actually first proposed in Ref. 85 for the case of electromagnetic waves. The snapshot of the surface waves for the homogenized coating is shown in Fig. 2.17(b), which is calculated by COMSOL Multiphysics. The stream lines indicating the direction of the fluid flow, clearly demonstrate the bending effect in the cloaking area.

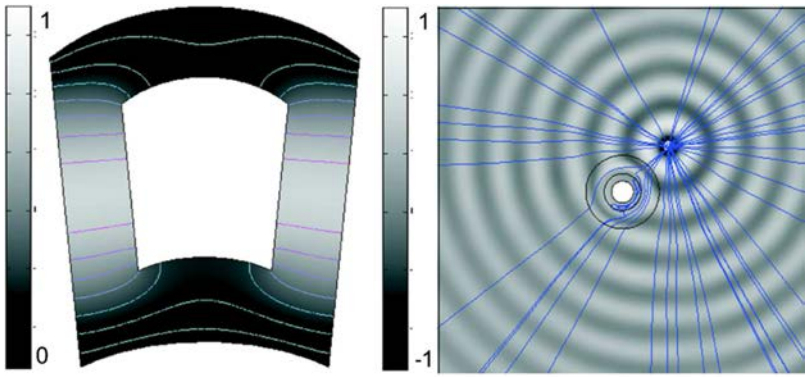

Fig. 2.17. (a) Calculated periodic hydrostatic field. (b) Pattern of the concentric surface wave and associated stream lines (indicating the direction of fluid flow) generated by a forced term with frequency 15.84 Hz. A rigid cylinder of radius 38 mm is placed in the center of a homogenized cloak.[74]

Similar approaches are applied for acoustic wave and electromagnetic wave as well. The homogenized wave equations (in polar coordinates) for acoustic waves can be written as:

$$-\nabla \cdot \left(\begin{bmatrix} \rho_{rr}^{-1} & 0 \\ 0 & \rho_{\theta\theta}^{-1} \end{bmatrix} (r) \nabla p(r,\theta) \right) = \frac{\omega^2}{K_{eff}} p(r,\theta) \tag{2.55}$$

where the tensor of effective density is given by

$$\begin{bmatrix} \rho_{rr}^{-1} & 0 \\ 0 & \rho_{\theta\theta}^{-1} \end{bmatrix} = \frac{1}{\text{area}(Y)} \int_0^{2\pi} \int_0^1 \rho(r,r',\theta') \times \begin{bmatrix} \text{area}(Y) - \psi_{rr} & \psi_{r\theta} \\ \psi_{\theta r} & \text{area}(Y) - \psi_{\theta\theta} \end{bmatrix} r' dr' d\theta' \tag{2.56}$$

Here, ψ_{ij} are periodic potentials.

And for electromagnetic wave:

$$-\nabla \cdot \left(\begin{bmatrix} \epsilon_{rr}^{-1} & 0 \\ 0 & \epsilon_{\theta\theta}^{-1} \end{bmatrix} (r) \nabla H_z(r,\theta) \right) = \omega^2 \mu_{eff} H_z(r,\theta) \tag{2.57}$$

where ϵ_{rr}^{-1} and $\epsilon_{\theta\theta}^{-1}$ are the coefficients of the tensor of effective permittivity which are also given by Eq. (2.56) (replacing ρ by μ in the equation) and μ_{eff} is the effective permeability which can be written as:

$$\mu_{eff} = \frac{1}{\text{area}(Y)} \int_0^{2\pi} \int_0^1 \mu(r, r', \theta') r' dr' d\theta' \tag{2.58}$$

It is noted that this equation is simply derived from the vector Maxwell equation by considering a magnetic field $\mathbf{H} = (0, 0, H_z)$.

It can be shown that the reduced effective parameters are good approximations for well-known transformed density and permittivity in their reduced forms:

$$\rho'_{rr} = \left(\frac{R_2(r - R_1)}{r(R_2 - R_1)}\right)^2, \quad \rho'_{\theta\theta} = \left(\frac{R_2}{R_2 - R_1}\right)^2 \tag{2.59}$$

$$\epsilon'_{rr} = \left(\frac{R_2(r - R_1)}{r(R_2 - R_1)}\right)^2, \quad \epsilon'_{\theta\theta} = \left(\frac{R_2}{R_2 - R_1}\right)^2 \tag{2.60}$$

The numerical simulation for all these three cases are conducted by using the commercial finite elements package COMSOL Multiphysics. The geometric configuration in the simulation is same as the real structured cloaking device. Here, we select electromagnetic wave as an example to demonstrate the invisible cloak behavior as shown in 2.18. In order to quantitatively assess the cloaking efficiency of the metamaterial, we numerically compute its total radar cross section (RCS),[86,87] and plot them in Fig. 2.18(d). We can observe that a small infinite conducting (resp. rigid for pressure waves) obstacle surrounded by the cloak is slightly above RCS of the cloak on its own, but lower than RCS of small infinite conducting (resp. rigid) obstacle, which is itself smaller than RCS of the large infinite conducting (resp. rigid) obstacle of same diameter as the cloak up to 7 GHz (resp. 8 KHz for pressure waves). The theoretical and numerical results confirm that these two-dimensional finite element simulations are valid for all water wave, acoustic wave, and transverse electromagnetic wave.

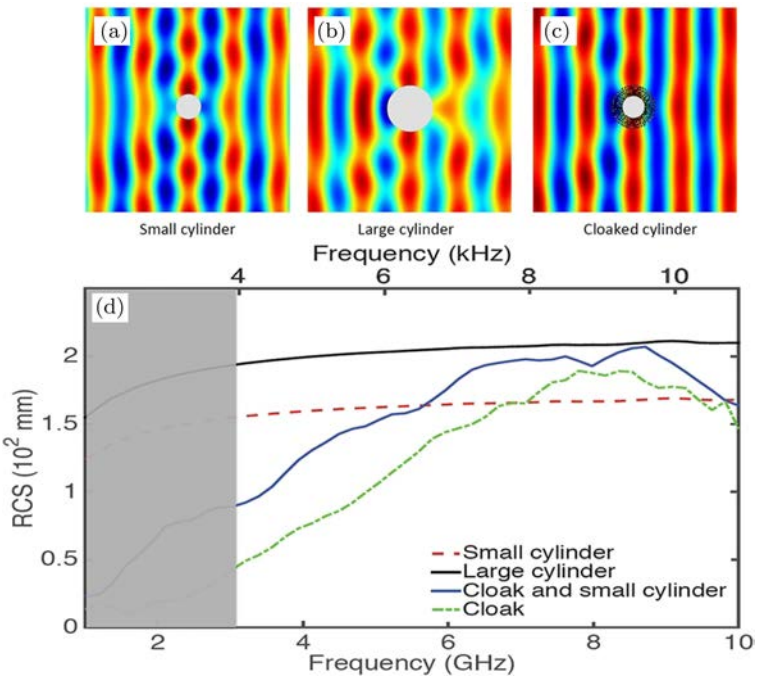

Fig. 2.18. The simulated real part of the transverse magnetic (resp. pressure) field for a plane wave incident at 4.5 GHz (resp. 5 kHz) from the left on the small obstacle surrounded by the cloak on the small obstacle on its own (a), on the large obstacle (b), and on the cloaked obstacle (c). (d) Numerical simulation of radar cross section (RCS) for cloak and cylindrical rigid obstacles.[81]

2.3.3.3. *Experimental characterization*

The performance of the invisible cloak has been characterized for water, acoustic, and electromagnetic waves, respectively. In Fig. 2.19 (a), we present the schematic experimental setup for observing back scattering water wave from the cloak. In the system, a halogen lamp modulated by a perforated rotating disc illuminates a transparent vessel containing the liquid. We choose a small tube to excite a localized pressure with the same frequency as the modulation of the light. The surface waves create local curvatures of the liquid and the light is refracted when crossing the surface. Therefore, on the screen the dark and light zones allow visualizing the liquid surface waves. We

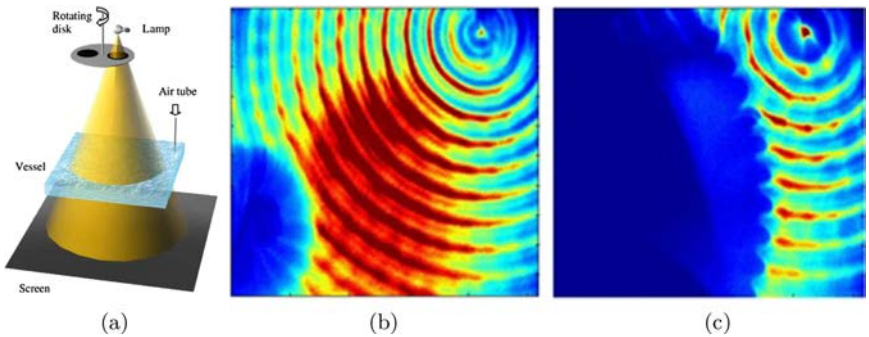

Fig. 2.19. Schematic view of the experimental setup for linear surface water waves. (b–c) Experimental results of reduced backscattering adapted from[74] for a concentric liquid surface wave of frequency 10 Hz interacting with a rigid cylinder (7.6 cm in diameter) on its own (b) and the structured waterwave cloak (20 cm in diameter) (c).[81]

take snapshots of the liquid surface waves when a metallic cylinder is placed in the vessel alone and with the invisibility cloak, which are shown in Fig. 2.19(b) and (c). The dramatic reduced back scattering field can be observed if the metallic cylinder is placed in the cloak.

The schematic view of acoustic wave experimental setup is shown in Fig. 2.20(c). A commercial loudspeaker is placed at 20 cm from the structure cloak. The loudspeaker is driven by a programmable functional generator and a power amplifier. A high sensitive microphone mounted on an x-y translation stage is used to record the two-dimensional acoustic pressure field distribution. The loudspeaker, acoustic cloak, and microphone are placed at the same level for characterizing how the pressure field is affected by the cloak. In the experiment, a five-period sinusoidal wave is launched by the loudspeaker. The time-dependent pre-amplified signal collected by the microphone is recorded by an oscilloscope and downloaded to a computer for further analysis. The signal generation and acquisition are synchronized by the computer program. Therefore, we can map the 2D pressure field distribution with both amplitude and phase information. The scanning area is 25×25 cm^2. The measured forward scattering fields for a cylindrical scatterer with or without the cloak are plotted in Fig. 2.20(a). We can observe that the acoustic wavefront is neatly

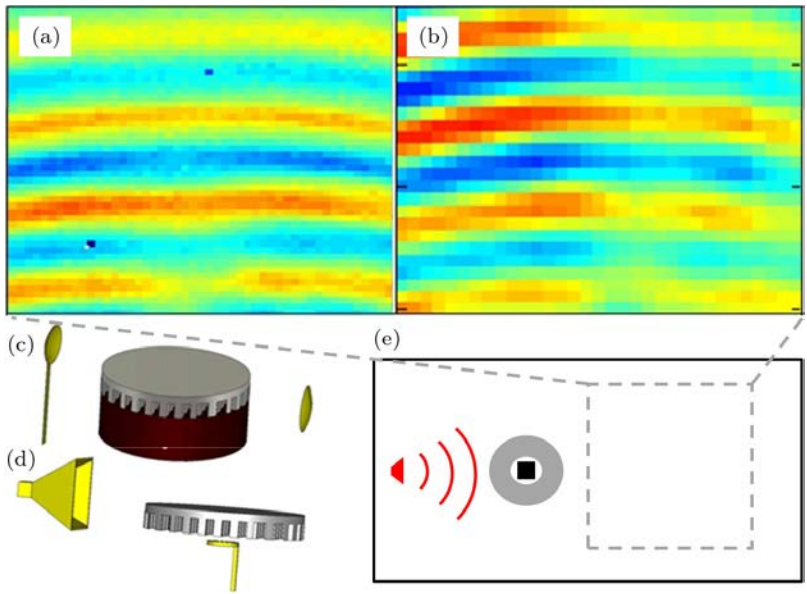

Fig. 2.20. (a, b) Experimental results in forward scattering for pressure waves (a) and transverse electric microwaves (b) for the same cloak containing a large glass bottle obstacle (a) and a small square metallic obstacle (b). (c, d) Schematic view of the experimental setup for acoustic wave (c) and microwave (d). (e) Top view of 2D configuration for forward scattering wave mapping. The measured area are indicated by the dashed box.

reconstructed behind the cloak, with a good agreement with the numerical simulation results.

The schematic view of microwaves experimental setup which is positioned in an anechoic chamber is shown in Fig. 2.20(d). A ridged horn antenna is positioned at 24 cm from the structure cloak. A rectangular metallic obstacle is inside the cloak structure. The magnetic probe is positioned 5 mm above the structure cloak. The probe is a homemade magnetic loop with diameter 5 mm and the loop is positioned perpendicular to the magnetic field of the emitter antenna. In this configuration, the magnetic probe measures a single component (vertical component) of the three Cartesian components of the magnetic field. The magnetic loop scanned a 33×71 cm^2 surface thanks to a 3D axis positioning system.[86] The antenna and the probe

are connected to a vector network analyzer that generates and measures the electromagnetic field. The electromagnetic field is emitted by the antenna and the probe only receives the field. The vector network analyzer measures the transmission coefficient between the emitter antenna and the magnetic probe. The complex transmission coefficient between the antenna and the probe is displayed in terms of magnitude in dB to visualize the intensity of the field. The real part of the magnetic field is also displayed since this is related to the phase of the field. The measured forward scattering longitudinal magnetic field for a square metallic obstacle placed in the cloak is plotted in Fig. 2.20(b). Similar to the results of the acoustic wave, the electromagnetic wavefront is reconstructed.

In conclusion, we present three experiments demonstrating that a cylindrical cloak works equally well for linear surface liquid wave, acoustic wave, and electromagnetic wave. Measured forward scattering for pressure and magnetic fields are in good agreement and confirm broadband cloaking with a central frequency of 5 kHz for sound and 4.3 GHz for microwaves. Microwave experiments further confirm the much reduced forward and backscattering when a rectangular metallic obstacle is surrounded by the structured cloak range of cloaking frequencies between 2.6 and 6.0 GHz. This suggests, as supported by numerical simulations, sound waves are cloaked between 3 and 7 kHz and linear surface liquid waves are cloaked between 8 to 14 Hz. Moreover, microwave experiments confirm the field is reduced by 10 to 30 dB inside the invisibility region, which suggests the multiphysics cloak could be used as a protection against water, sonic or microwaves.

2.3.4. *Anisotropic complementary acoustic complementary metamaterials*

In the previous sections, we have introduced conventional cloaking strategies[50,74,88] by compressing the space and hide the object inside an enclosure in which there is no interaction with the outside world. However, this solution is not suited to the problems for

the application of medical ultrasound or non-destructive evaluation (NDE). In these problems, ultrasound needs to be transmitted through an aberrating layer,[89–95] where either the transmission is desired to be maximized or the reflection needs to be minimized. One of the most representative examples is transcranial ultrasound beam focusing, which could find usage in both brain imaging and treatment.[91,92] However, transcranial beam focusing is extremely challenging due to the presence of the skull. A common approach to achieve transcranial beam focusing is based on the time-reversal/phase conjugate technique and ultrasound phased arrays.[96,97] Although the focal position can be corrected, one significant shortcoming of this strategy is that it does not compensate for the large acoustic energy loss due to the impedance mismatch between the skull and the background medium (water). Recently, Lai *et al.* demonstrated that cloaking/illusion based on electromagnetic wave (EM) complementary metamaterials (CMM)[98] can open up a virtual hole in a wall without distortion.[99,100] In addition, this type of approach does not require the cloaked object to be inside an enclosure/cloaking shell and is valid in free space.[101] Due to the similarity between acoustic and EM wave equations in 2D, CMMs have been also proposed for acoustic cloaking.[102,103]

In this section, we will introduce a type of anisotropic, acoustic complementary metamaterials (CMM) and their application in restoring acoustic fields distorted by aberrating layers.[104] The proposed quasi 2D, non-resonant CMM consists of unit cells formed by membranes and side branches with open ends. Simultaneously anisotropic and negative density is achieved by assigning membranes facing each direction (x- and y-direction) with different thicknesses while the compressibility is tuned by the side branches. Numerical examples demonstrate that, the CMM, when placed adjacent to a strongly aberrating layer, could acoustically cancel out that aberrating layer. This leads to dramatically reduced acoustic field distortion and enhanced sound transmission, therefore virtually removing the layer in a noninvasive manner.

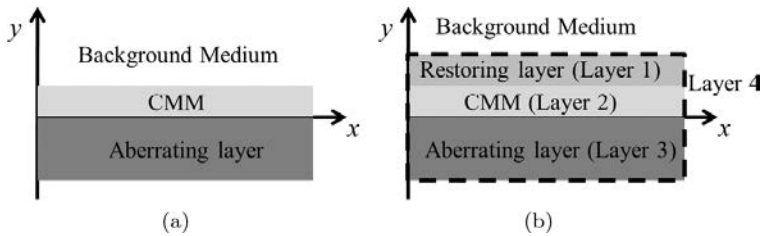

Fig. 2.21. (a) Schematic of the CMM, the aberrating layer, and the background medium. (b) Schematic of acoustic cloaking using CMM, the dashed lines indicate the boundaries of layer 4.

2.3.4.1. *Theoretical approach for CMM*

The CMM is placed on top of the aberrating layer, as illustrated in Fig. 2.21(a). The aberrating layer is assumed to be sufficiently long so that the edges do not significantly affect the acoustic field. The CMM compresses and cancels the information of the selected aberrating layer. Let $\rho^{(c)}(x^{(c)}, y^{(c)}, z^{(c)})$, $\chi^{(c)}(x^{(c)}, y^{(c)}, z^{(c)})$ and $\rho^{(a)}(x^{(a)}, y^{(a)}, z^{(a)})$, $\chi^{(a)}(x^{(a)}, y^{(a)}, z^{(a)})$ be the effective density and compressibility tensors of the CMM and the aberrating layer, respectively. $x^{(c)}, y^{(c)}, z^{(c)}$ and $x^{(a)}, y^{(a)}, z^{(a)}$ are generalized curved coordinates. Based on the acoustic coordinate transformation, we have[69]:

$$\left[\rho^{(c)}\right]^{-1} = \mathbf{A}\left[\rho^{(a)}\right]^{-1}\mathbf{A}^{T}/\det\mathbf{A}, \tag{2.61}$$

$$\chi^{(c)} = \chi^{(a)}/\det\mathbf{A}, \tag{2.62}$$

where $\mathbf{A}$ is the Jacobian transformation tensor of compressing transformation given by:

$$\mathbf{A} = \begin{bmatrix} \frac{\partial x^{(c)}}{\partial x^{(a)}} & \frac{\partial x^{(c)}}{\partial y^{(a)}} & \frac{\partial x^{(c)}}{\partial z^{(a)}} \\ \frac{\partial y^{(c)}}{\partial x^{(a)}} & \frac{\partial y^{(c)}}{\partial y^{(a)}} & \frac{\partial y^{(c)}}{\partial z^{(a)}} \\ \frac{\partial z^{(c)}}{\partial x^{(a)}} & \frac{\partial z^{(c)}}{\partial y^{(a)}} & \frac{\partial z^{(c)}}{\partial z^{(a)}} \end{bmatrix} \tag{2.63}$$

In this study, we focus on 2D problems and only wave propagation in the x-y plane is of interest. The z component in the Jacobian

matrix is therefore dropped. Without loss of generality, the thickness of the CMM is assumed to be half of the aberrating layer, which leads to $\frac{\partial x^{(c)}}{\partial x^{(a)}} = 1$ and $\frac{\partial y^{(c)}}{\partial y^{(a)}} = -0.5$, whose ratio is negative since the acoustic information is folded in the CMM and would cancel out that of the aberrating layer. Other components $\frac{\partial x^{(c)}}{\partial y^{(a)}}$ and $\frac{\partial y^{(c)}}{\partial x^{(a)}}$ in the tensor are equal to zero, as the transformation in each direction (i.e., x- and y-directions) are independent. For more complicated geometries, off-diagonal components may appear. They could, however, be eliminated by coordinate rotations.[105]

Finally, the tensor $\mathbf{A} = \begin{pmatrix} 1 & 0 \\ 0 & -0.5 \end{pmatrix}$, and consequently, the density and compressibility tensors of the CMM are: $\rho^{(c)} = \begin{pmatrix} -0.5 & 0 \\ 0 & -2 \end{pmatrix} \times \rho^{(a)}$ and $\chi^{(c)} = -2 \times \chi^{(a)}$. It is noted that a generalized CMM requires strongly anisotropic density as well as negativity for both density and compressibility. In addition, the density can be isotropic if the thickness of the CMM is chosen to be the same as the aberrating layer. However, in this case, the refractive index is -1 and the k vector along the interface goes to infinity.[106] In other words, such a CMM will be very sensitive to the unit cell size and can be difficult to demonstrate. Furthermore, a generalized CMM is preferred in practice as its thickness can be arbitrarily chosen, i.e., it does not depend on the thickness of the aberrating layer, providing a great flexibility.

2.3.4.2. *Unit cell design for CMM*

Periodic cubic blocks with clamped elastic membranes and side branches as shown in Fig. 2.22 are chosen to achieve the double negative and anisotropic properties for CMM. The membrane is introduced here to tune the effective density. The side branches are open ended and are introduced to tune the effective compressibility. In the demonstration, we choose the operating frequency of the CMM to be 50 kHz, at which the wavelength in water (background medium) is 15 times larger than the size of a unit cell. By adjusting the thicknesses of the membranes facing each direction (x- and y-), the effective density can be tuned therein in order to achieve anisotropy. Assuming the interaction and coupling between membranes in the

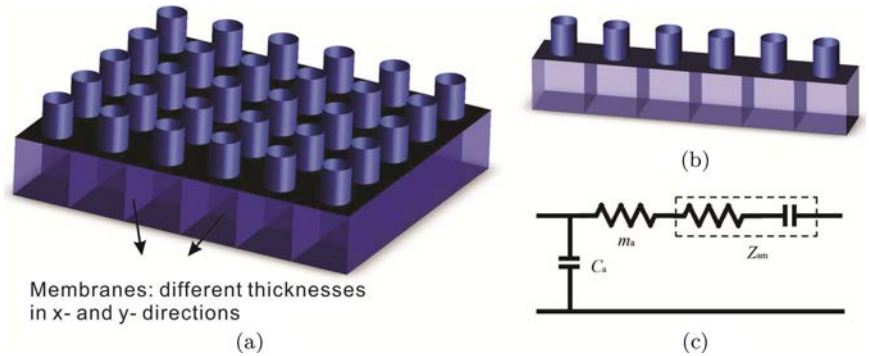

Fig. 2.22. (a) Schematic of a portion of the quasi 2D CMM. (b) Schematic of a 1D side brand and membrane-based metamaterial. (c) Equivalent acoustic circuit of the 1D membrane-based metamaterial.

x- and y- directions is negligible, the effective density and compressibility in either x- or y- direction can be estimated separately by one dimensional (1D) studies.[107] To this end, 1D models are first studied in order to determine the appropriate thicknesses of the membranes and the dimensions of the side branches by both theoretical analysis and numerical simulations (Fig. 2.22(b)).

Theoretically, the effective compressibility with open ended side branches in theory can be written as[108]: $\chi_e = \chi_0(1 - \frac{S}{Ad\rho_0\beta_0 l'\omega^2})$, where β_0 is compressibility of the background medium, S, A, d, l' are, respectively, cross section area of the branch, cross section area of the waveguide (cubic block), length of unit cell, the effective length of the branch, and is the angular frequency. On the other hand, the effective density of the unit cell depends on the properties of the membranes.[108–111] The side branches are assumed to have negligible effect on the effective density.[108] The effective density with clamped membranes can be derived by using the lumped model, with the equivalent acoustic circuit of the 1D membrane-based metamaterial shown in Fig. 2.22(c). Here, $m_a = \frac{\rho_0}{A(d-h)}$ is the effective acoustic mass of the tube, $C_a = A\chi_0(d-h)$ is the acoustic capacitance of the waveguide, where h is the membrane thickness. Z_{am} is the acoustic impedance of the membrane and can be approximated by an inductor

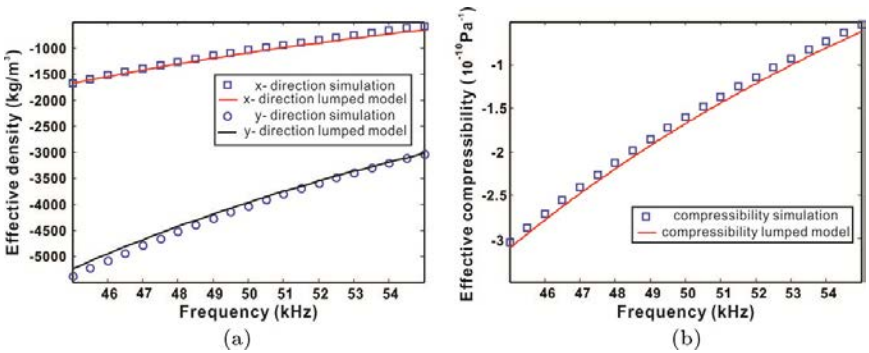

Fig. 2.23. Effective densities and compressibility extracted from full wave simulations and predicted by the lumped model.[104] (a) Effective densities in x- and y-directions. (b) Effective compressibility. At 50 kHz, the desired density and compressibility are achieved.

and capacitor in series in the low-frequency region,[109] and defined as:

$$Z_{am} = \frac{Z_m}{A^2} = \frac{\iint \Delta p dA}{j\omega\xi A^2}, \tag{2.64}$$

where $\Delta p = p_1 - p_2$ is the pressure difference across the membrane, Z_m is the mechanical impedance of the membrane and ξ represents the average displacement of the membrane. Therefore, the expression for the total acoustic impedance of the tube is: $Z_{as} = j\omega m_a + Z_{am}$, with the effective density of a unit cell written as: $\rho_e = \frac{Z_{as}}{j\omega}\frac{1}{dA}$.

The effective acoustic parameters calculated by theoretical prediction are compared with the numerical simulation by COMSOL Multiphysics, which are shown in Fig. 2.23. We can observe a good agreement. We need to address that negative properties of these structures are not relying on the resonance, since the negative properties appear in a broad-band frequency range. The material properties and geometric parameters in the simulation are listed: the membrane made by aluminum film is 2 mm × 2 mm; the Young's modulus is 70 GPa; the Poisson's ratio is 0.33; the density is 2700 kg/m^3; the thicknesses of the membranes are 0.083 mm and 0.11 mm in x and y directions; the radius and length of the side branches are 0.25 mm and 1.25 mm. The density and sound speed of background medium (water) are 1000 kg/m^3 and 1500 m/s.

2.3.4.3. *Numerical simulation*

We conduct two sets of full wave simulation to validate the designed CMM by using COMSOL Multiphysics. The acoustic-solid interaction module is chosen for numerical simulations. The entire CMM consists of 120×10 unit cells: there are 120 units along x-direction and 10 units along y-direction. Perfectly matched layers (PML) are used to minimize reflections from the boundary. The thickness of the aberrating layer is 40 mm, with the material density 2000 kg/m^3 and sound speed 2500 m/s, for mimicking human skulls. The acoustic impedance of aberrating layer is therefore over 3.3 times larger than the background medium, providing a sufficient amount of mismatch. According to the effective material property calculation, the effective density of the unit cells are -1000 kg/m^3 (along x-axis) and -4000 kg/m^3 (along y-axis), as well as the effective compressibility is -1.6×10^{-10} m^2/N, which meet the requirement of the coordinate transformation.

In the two simulations, we configure a curved/focused array and a linear array to generate different acoustic fields. In the first case, the curved acoustic source array which can generate a focal point in the free space (shown in Fig. 2.24(b) as a control case) is placed in front of the aberrating layer. It is straightforward that the aberrating layer can block most of the transmission acoustic energy due to the large impedance mismatch, as shown in Fig. 2.24(a). By placing the CMM layer on the same side with the array, the CMM can effectively cancel out the aberrating layer, so a strong focal point which is 60 mm (total thickness of the CMM and the aberrating layer) behind the original one can be observed. The curved source array is moved 60 mm away from the aberrating layer when the CMM is inserted, so that the focal point remains at the desired location, as shown in Fig. 2.24(c). Quantitative analysis shows that in the curved array case, the intensity amplitude at the focal point is 88% of that of the control case, while it is 28% without the CMM. A significant improvement in terms of the sound transmission ($> 300\%$) is achieved. As indicated in the white dash line in Fig. 2.24(c), the focal point of the CMM case results in an accurate position, which is only 3 mm (1/10 of

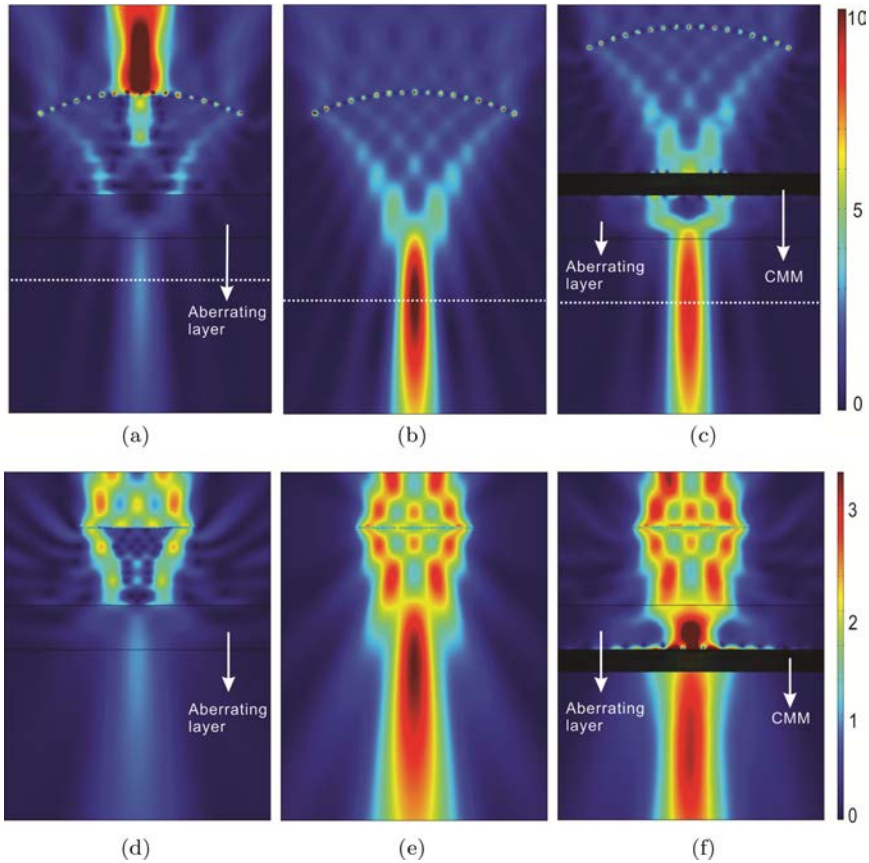

Fig. 2.24. (a–c) Acoustic intensity field for a curved array (focused beam). The CMM is placed in front of the aberrating layer. White dotted lines indicate the position of the focal plane. Three cases are presented: (a) Skull only. (b) Homogeneous medium. (c) With CMM and skull. (d–f) Acoustic intensity field for a linear array (unfocused beam). The CMM is placed behind the aberrating layer. Three cases are presented: (d) Skull only. (e) Homogeneous medium. (f) With CMM and skull.[104]

the wavelength) off the desired location as in the control case, while it is 14 mm (about 1/2 of the wavelength) off without the CMM. This example demonstrates one potential application of CMMs to focus ultrasound behind aberrating layers, which could be extremely useful for improving ultrasound imaging or therapy. In the linear

array case (unfocused acoustic field), which we place the CMM layer behind the aberrating layer, the total acoustic intensity is 97% of that of the control case, whereas the transmission is only 31% without the CMM. The numerical simulation results are plotted in Fig. 2.24(d–f). This example demonstrates another potential application of CMMs to detect passive acoustic source emissions or reflections from an object to be imaged/detected behind aberrating layers. Also, interestingly, this example indicates that the CMM can be placed behind a reflective layer and yet achieve anti-reflection, thus has the advantage of being virtually concealed.

In both cases, the effective density and compressibility are extracted from the simulation results and are very close to the ones predicted by the earlier 1D model. It is noted that in ideal case, the CMM should exactly restore the sound field without considering the energy loss inside the metamaterial. However, it would require an infinitely small unit cell so that the homogenization is perfect. In the current simulation, the material losses are not taken into account in the simulations, since aluminum (membrane material) is known to have a small loss factor and the attenuation in water is also negligible. In addition, the side branch and membrane-based metamaterials used here are non-resonant metamaterials,[108] therefore the material loss is not expected to be a significant factor.

A single CMM layer can significantly enhance the acoustic energy transmission through the aberrating layer. However, the phase of the acoustic field cannot be recovered, which induces the focal point shift in the curved source array case. Similar to the electromagnetic CMMs, an additional restoring layer added on top of the CMM layer can recover both amplitude and phase information of the acoustic field to achieve an acoustic cloaking. The same mathematics of coordinate transformation is applied to retrieve the effective parameters for layer 1 and 2. The effective density and compressibility tensors for layer 2 are the same as the previous result, since layer 2 plays the same function to cancel out the aberrating layer. Layer 1 will restore the information of layer 4 (combine with layer 1, 2, and 3), which has the acoustic properties of the background medium.

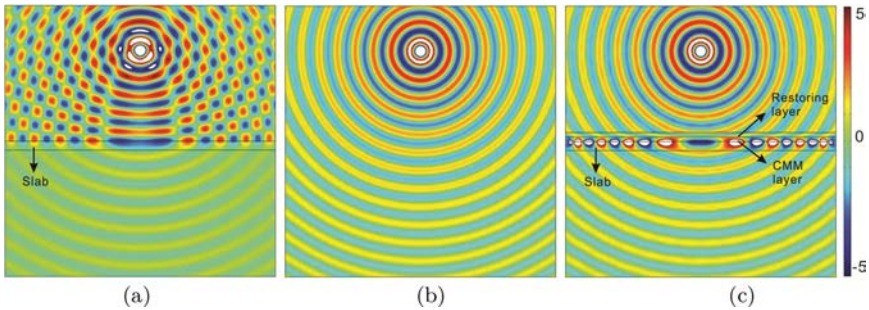

Fig. 2.25. (a–c) Acoustic pressure filed for a point source which is blocked by a slab. An acoustic cloaking device is placed on top of the slab so that it can effectively cloak the slab.[104] (a) Slab only. (b) Homogeneous medium. (c) With cloaking device adjacent to the slab. The wave fields in (b) and (c) are almost identical.

Therefore, the effective density and compressibility tensors for layer 1 are $\rho^{(1)} = \begin{pmatrix} 0.25 & 0 \\ 0 & 4 \end{pmatrix} \times \rho_0$ and $\chi^{(1)} = 4 \times \chi_0$. We conduct the numerical simulation by using the homogenized effective media with desired properties, and plot them in Fig. 2.25. The simulation results show that a slab is effectively cloaked by the cloaking device with a CMM layer and a restoring layer.

In conclusion, we design acoustic CMMs based on the coordinate transformation of acoustic waves to cancel out an object in free space. Numerical examples demonstrate that the CMMs are able to restore the acoustic fields distorted by aberrating layers, which is capable of virtually removing an aberrating layer in a non-invasive manner. Therefore, it could greatly facilitate NDE, transcranial ultrasound imaging and treatment. In addition, the method for designing acoustic CMMs can be readily used to cancel out multiple layers if needed. CMMs are also expected to be useful for the design of acoustic cloaking and all angle anti-reflection materials.[112,113]

Bibliography

[1] Liu, Z., *et al.* (2000). *Science* **289**, p. 1734.
[2] Li, J. and Chan, C. T. (2004). *Phys. Rev. E* **70**, p. 055602.

[3] Fang, N., Xi, D., Xu, J., Ambati, M., Srituravanich, W., Sun, C. and Zhang, X. (2006). *Nature Mater.* **5**, pp. 452–456.
[4] Cheng, Y., *et al.* (2008). *Appl. Phys. Lett.* **92**, p. 051913.
[5] Mei, J., *et al.* (2006). *Phys. Rev. Lett.* **96**, p. 024301.
[6] Ding, Y. Q., *et al.* (2007). *Phys. Rev. Lett.* **99**, p. 093904.
[7] Hu, X. H. and Chan, C. T. (2005). *Phys. Rev. E* **71**, p. 055601.
[8] Sheng, P. (1995). *Introduction to Wave Scattering, Localization and Mesoscopic Phenomena*, Academic, New York.
[9] Ye, Z. and Hsu, H. (2001). *Appl. Phys. Lett.* **79**, p. 1724.
[10] Wang, Z. G., *et al.* (2008). *J. Appl. Phys.* **103**, p. 064907.
[11] Cheng, Y., *et al.* (2008). *Phys. Rev. B* **77**, p. 045134.
[12] Lai, A., *et al.* (2004). *Microwave. Mag. IEEE* **5**, p. 34.
[13] Zhang, S., Yin, L. and Fang, N. X. (2009). *Phys. Rev. Lett.* **102**, p. 194301.
[14] Fokin, V., *et al.* (2007). *Phys. Rev. B* **76**, p. 144302.
[15] Hou, Z., *et al.*, (2005). *Phys. Rev. E* **71**, p. 037604.
[16] Pendry, J. B., Schurig, D. and Smith, D. R. (2006). *Science* **312**, p. 1780.
[17] Leonhardt, U. (2006). *Science* **312**, p. 1777.
[18] Kildishev, A. V. and Shalaev, V. M. (2008). *Opt. Lett.* **33**, p. 43.
[19] Rahm, M., Cummer, S. A., Schurig, D., Pendry, J. B. and Smith, D. R. (2008). *Phys. Rev. Lett.* **100**, p. 063903.
[20] Schurig, D. *et al.* (2006). *Science* **314**, pp. 977–980.
[21] Rahm, M. *et al.* (2008). *Opt. Express* **16**, p. 11555.
[22] Smith, D. R., Padilla, W. J., Vier, D. C., Nemat-Nasser, S. C. and Schultz, S. (2000). *Phys. Rev. Lett.* **84**, p. 4184.
[23] Smith, D. R., Pendry, J. B. and Wiltshire, M. C. K. (2004). *Science* **305**, pp. 788–792.
[24] Nemati, N., Kumar, A., Lafarge, D. and Fang, N. X. (2015). *Comptes Rendus*, doi:10.1016/j.crme.2015.05.001.
[25] Maznev, A., Gu, G., Sun, S., Xu, J., Shen, Y., Fang, N. and Zhang, S. (2015). *New Journal of Physics* **17**(4), p. 042001.
[26] Pendry, J. B., Holden, A. J., Robbins, D. J. and Stewart, W. J. (1999). *IEEE Trans. Microw. Theory Tech.* **47**, pp. 2075–2084.
[27] Iyer, A. K., Kremer, P. C. and Eleftheriades, G. V. (2003). *Opt. Express* **11**, pp. 696–708.
[28] Lafarge, D. and Nemati, N. (2013). *Wave Motion* **50**, pp. 1016–1035.
[29] Zwikker, C. and Kosten, C. W. *Sound Absorbing Materials*, Elsevier Publishing company, Inc., New York (1949). Reprinted 2012 by the NAG (Nederlands Akoestisch Genootschap).
[30] Johnson, D. L., Koplik, J. and Dashen, R. (1987). *J. Fluid Mech.* **176**, pp. 379–402.
[31] Champoux, Y. and Allard, J. F. (1991). *J. Appl. Phys.* **70**, pp. 1975–1979.
[32] Lafarge, D., Lemarinier, P., Allard, J. F. and Tarnow, V. (1997). *J. Acoust. Soc. Am.* **102**, pp. 1995–2006.
[33] Burridge, R. and Keller, J. B. (1981). *J. Acoust. Soc. Am.* **70**, pp. 1140–1146.

[34] Norris, A. N. (1986). *J. Wave Mat. Interact.* **1**, pp. 365–380.
[35] Zhou, M. Y. and Sheng, P. (1989). *Phys. Rev. B* **39**, pp. 12027–12039.
[36] Smeulders, D. M. J., Eggels, R. L. G. M. and van Dongen, M. E. H. (1992). *J. Fluid Mech.* **245**, pp. 211–227.
[37] Auriault, J. L. (1980). *Int. J. Engng Sci.* **18**, pp. 775–785.
[38] Auriault, J. L., Boutin, C. and Geindreau, C., *Homogenization of Coupled Phenomena in Heterogenous Media*, ISTE and Wiley (2009).
[39] Sanchez Palencia, E., *Nonhomogeneous Media and Vibration Theory*, Lectures notes in Physics, 127, Springer, Berlin (1980).
[40] Bensoussan, A., Lions, J. L. and Papanicolaou, G. C., *Asymptotic Analysis for Periodic Structure*, North-Holland, Amsterdam (1978).
[41] Craster, R. V., Kaplunov, J. and Pichugin, A. V. (2010). *Proc. R. Soc. A* **466**, pp. 2341–2362.
[42] Antonakakis, T., Craster, R. V., Guenneau, S. and Skelton, E. A. (2013). *Proc. R. Soc. A* **470**, p. 20130467.
[43] Boutin, C., Rallu, A. and Hans, S. (2012). *J. Acoust. Soc. Am.* **132**, pp. 3622–3636.
[44] Boutin, C. (2013). *J. Acoust. Soc. Am.* **134**, pp. 4717–4729.
[45] Yang, M., Ma, G., Wu, Y., Yang, Z. and Sheng, P. (2014). *Phys. Rev. B* **89**, p. 064309.
[46] Wu, Y., Lai, Y. and Zhang, Z. Q. (2007). *Phys. Rev. B* **76**, p. 205313.
[47] Boutin, C. (2012). *Transp. Porous Med.* **93**, pp. 309–329.
[48] Willis, J. R. (2009). *Mech. Mater.* **41**, pp. 385–393.
[49] Landau, L. D. and Lifshitz, E. M., *Electrodynamics of Continuous Media*, Course of Theoretical Physics Vol. 8 Elsevier, Oxford/Butterworth-Heinemann (2004).
[50] Zhang, S., Xia, C. and Fang, N. (2011). *Phys. Rev. Lett.* **106**, p. 24301.
[51] Nemati, N. and Lafarge, D. (2014). *Wave Motion* **51**, pp. 716–728.
[52] Allard, J. F. and Atalla, N., *Propagation of Sound in Porous Media: Modelling Sound Absorbing Materials*, Second Edition, John Wiley & Sons (2009).
[53] Hecht, F. (2012). New development in FreeFem++, *J. Numer. Math.* **20**, pp. 251–265.
[54] Veselago, V. G. (1968). *Sov. Phys. Usp.* **10**(4), p. 509.
[55] Pendry, J. B. (2000). *Phys. Rev. Lett.* **85**, p. 3966.
[56] Fang, N., Lee, H., Sun, C. and Zhang, X. (2005). *Science* **308**, p. 534.
[57] Grbic, A. and Eleftheriades, G. V. (2004). *Phys. Rev. Lett.* **92**, p. 117403.
[58] Kinsler, L. E., *Fundamentals of Acoustics*, Wiley, New York (1982).
[59] Stewart, G. W. (1922). *Phys. Rev.* **20**, p. 528.
[60] Mason, W. P. (1927). *Bell Syst. Tech. J.* **6**, p. 258.
[61] Eleftheriades, G. V., Iyer, A. K. and Kremer, P. C. (2002). *IEEE Trans. Microwave Theory Tech.* **50**, p. 2702.
[62] Beranek, L. L., *Acoustics*, McGraw-Hill, New York (1954).
[63] Lemoult, F., Fink, M. and Lerosey, G. (2011). *Phys. Rev. Lett.* **107**, p. 064301.

[64] Bruneau, M. (2006). *Fundamentals of Acoustics* (London: ISTE).
[65] Ward, A. J. and Pendry, J. B. (1996). *Journal of Modern Optics* **43**(4), pp. 773–793.
[66] Stenger, N., Wilhelm, M. and Wegener, M. (2012). *Phys. Rev. Lett.* **108**, p. 014301.
[67] Milton, G. W., Briane, M. and Willis, J. R. (2006). *New Journal of Physics* **8**(10), p. 248.
[68] Cummer, S. A. and Schurig, D. (2007). *New Journal of Physics* **9**(3), p. 45.
[69] Chen, H. and Chen, C. T. (2007). *Applied Physics Letter* **91**(8).
[70] Li, J. and Pendry, J. B. (2008). *Phys. Rev. Lett.* **101**, p. 203901.
[71] Ergin, T., Stenger, N., Brenner, P., Pendry, J. B. and Wegener, M. (2010). *Science* **328**, pp. 337–339.
[72] Chen, X, *et al.* (2011). *Nat. Commun.* **2**, p. 176.
[73] Landy, N. and Smith, D. R. (2013). *Nature Mater.* **12**, pp. 25–28.
[74] Farhat, M., Enoch, S., Guenneau, S. and Movchan, A. B. (2008). *Phys. Rev. Lett.* **101**, p. 134501.
[75] Popa, B.-I., Zigoneanu, L. and Cummer, S. A. (2011). *Phys. Rev. Lett.* **106**, p. 253901.
[76] Brun, M., Guenneau, S. and Movchan, A. B. (2009). *Appl. Phys. Lett.* **94**, p. 061903.
[77] Farhat M., Guenneau, S. and Enoch, S. (2009). *Phys. Rev. Lett.* **103**, p. 024301.
[78] Guenneau, S., Amra, C. and Veynante, D. (2012). *Opt. Express* **20**, pp. 8207–8218.
[79] Narayana, S. and Sato, Y. (2012). *Phys. Rev. Lett.* **108**, p. 214303.
[80] Schittny, R., Kadic, M., Guenneau, S. and Wegener, M. (2013). *Phys. Rev. Lett.* **110**, p. 195901.
[81] Xu, J., Jiang, X., Fang, N., Georget, E., Abdeddaim, R., Geffrin, J.-M., Sabouroux, P., Enoch, S. and Guenneau, S. (2015). *Scientific Reports* **5**, p. 10678.
[82] Cherkaev, A. (2000). *Variational Methods for Structural Optimization*, New York: Springer-Verlag.
[83] Milton, G. W., *The Theory of Composites*, Cambridge: Cambridge University Press (2001).
[84] Acheson, D. J., *Elementary Fluid Dynamics*, Oxford University Press, Oxford (1990).
[85] Cai, W., Chettiar, U. K., Kildiev, A. V. and Shalaev, V. M. (2007). *Nat. Photon.* **1**, p. 224.
[86] Georget, E., Abdeddaim, R. and Sabouroux, P. (2014). *IEEE Trans. Antennas Propag.* **56**, pp. 240–248.
[87] Knott, E. F., Shaeffer, J. F. and Tuley, M. T., *Radar Cross Section* (Raleigh: SciTech Publishing Inc, 2nd edition) (2004).
[88] Cummer, S., Popa, B.-I., Schurig, D., Smith, D., Pendry, J., Rahm, M. and Starr, A. (2008). *Phys. Rev. Lett.* **100**, p. 024301.

[89] Smith, S. W., Trahey, G. E. and von Ramm, O. T. (1986). *Ultrasound Med. Biol.* **12**, p. 229.
[90] Clement, G. T., White, P. J. and Hynynen, K. (2004). *Acoust. Soc. Am.* **115**, p. 1356.
[91] Ivancevich, N. M., Pinton, G. F., Nicoletto, H. A., Bennett, E., Laskowitz, D. T. and Smith, S. W. (2008). *Ultrasound Med. Biol.* **34**, p. 1387.
[92] Win, K. K., Wang, J. and Zhang, C. (2010). *5th IEEE Conf. Ind. Electron. Appl.* 1675.
[93] Demirli, R., Amin, M. G., Shen, X. and Zhang, Y. D. (2012). *Adv. Acoust. Vib.* 1.
[94] Jing, Y., Meral, F. C. and Clement, G. T. (2012). *Phys. Med. Biol.* **57**, p. 901.
[95] Wang, T. and Jing, Y. (2013). *Phys. Med. Biol.* **58**, p. 6663.
[96] Clement, G. T. and Hynynen, K. (2002). *Phys. Med. Biol.* **47**, p. 1219.
[97] Pernot, M., Aubry, J.-F., Tanter, M., Boch, A.-L., Marquet, F., Kujas, M., Seilhean, D. and Fink, M. (2007). *J. Neurosurg.* **106**, p. 1061.
[98] Pendry, J. B. and Ramakrishna, S. A. (2003). *J. Phys. Condens. Matter* **15**, p. 6345.
[99] Lai, Y., Chen, H., Zhang, Z.-Q. and Chan, C. (2009). *Phys. Rev. Lett.* **102**, p. 093901.
[100] Lai, Y., Ng, J., Chen, H., Han, D., Xiao, J., Zhang, Z.-Q. and Chan, C. (2009). *Phys. Rev. Lett.* **102**, p. 253902.
[101] Zhu, X., Liang, B., Kan, W., Zou, X. and Cheng, J. (2011). *Phys. Rev. Lett.* **106**, p. 014301.
[102] Liu, B. and Huang, J. P. (2009). *Eur. Phys. J. Appl. Phys.* **48**, p. 20501.
[103] Yang, J., Huang, M., Yang, C., Peng, J. and Chang, J. (2010). *Comput. Mater. Sci.* **49**, p. 9.
[104] Shen, C., Xu, J., Fang, N. and Jing, Y. (2014). *Phys. Rev. X* **4**, p. 041033.
[105] Popa, B.-I. and Cummer, S. A. (2011). *Phys. Rev. B* **83**, p. 224304.
[106] Ambati, M., Fang, N., Sun, C. and Zhang, X. (2007). *Phys. Rev. B* **75**, p. 195447.
[107] Park, C. M., Park, J. J., Lee, S. H., Seo, Y. M., Kim, C. K. and Lee, S. H. (2011). *Phys. Rev. Lett.* **107**, p. 194301.
[108] Lee, S. H., Park, C. M., Seo, Y. M., Wang, Z. G. and Kim, C. K. (2010). *Phys. Rev. Lett.* **104**, p. 054301.
[109] Bongard, F., Lissek, H. and Mosig, J. R. (2010). *Phys. Rev. B* **82**, p. 094306.
[110] Lee, S. H., Park, C. M., Seo, Y. M., Wang, Z. G. and Kim, C. K. (2009). *Phys. Lett. A* **373**, p. 4464.
[111] Jing, Y., Xu, J. and Fang, N. X. (2012). *Phys. Lett. A* **376**, p. 2834.
[112] Torrent, D. and Sánchez-Dehesa, J. (2007). *New J. Phys.* **9**, p. 323.
[113] Wang, Y., Deng, K., Xu, S., Qiu, C., Yang, H. and Liu, Z. (2011). *Phys. Lett. A* **375**, p. 1348.